# Eocene Gold Ore Formation at Muteh, Sanandaj-Sirjan Tectonic Zone, Western Iran: A Result of Late-Stage Extension and Exhumation of Metamorphic Basement Rocks within the Zagros Orogen

ROBERT MORITZ,[†]

*Section des Sciences de la Terre, Université de Genève, Rue des Maraîchers 13, 1205 Genève, Switzerland*

FEREYDOUN GHAZBAN,

*Faculty of Environment, University of Tehran, Ghods St 25, P.O. Box 14155-6135, Tehran, Iran*

AND BRAD S. SINGER

*Department of Geology and Geophysics, University of Wisconsin-Madison, 1215 West Dayton Street, Madison, Wisconsin 53706*

## Abstract

A multidisciplinary study including field geology, microstructure analysis, $^{40}Ar/^{39}Ar$ dating, and fluid inclusion microthermometry and Raman spectrometry has been carried out on the Muteh gold deposit located in a greenschist to amphibolite facies metamorphic rock complex of the Sanandaj-Sirjan tectonic zone, Zagros orogen, Iran. The Muteh gold deposit has been previously interpreted as genetically related to Precambrian granitic intrusions, as an exhalative hot-spring deposit related to Paleozoic rhyolitic-acidic tuffs, and to local metamorphic processes.

Host rocks of the gold deposit are predominantly schist and gneiss, and subsidiary amphibolite and quartzite, and are intruded by leucogranites. In the vicinity of the gold deposit, the metamorphic and granitic rocks display a subhorizontal mylonitic foliation, containing a northeast-oriented stretching lineation. Field investigations in one of the producing open pits show that the gold orebodies are controlled by northwest-oriented normal faults and joints, dipping to the northeast and the southwest, and crosscutting the ductile fabric of the host rocks. Both the ductile fabric of the host rocks and the gold ore-controlling brittle structures are interpreted to have formed within a single, continuous extensional event, which started with ductile deformation and gradually changed into brittle deformation. Hydrothermal alteration associated with ore formation consists of quartz, muscovite, pyrite, dolomite-ankerite, and albite, which crosscuts the ductile fabric and overprints the metamorphic minerals of the host rocks. Pyrite is the dominant opaque mineral and is the major phase associated with gold. Chalcopyrite, marcasite, bismuth, galena, sphalerite, and pyrrhotite are subsidiary to rare phases.

$^{40}Ar/^{39}Ar$ incremental-heating and in situ laser-ablation age data reveal a coherent sequence of cooling and hydrothermal events in the metamorphic complex hosting the Muteh gold deposit. Muscovite samples from the alteration zone and from one quartz vein from the orebodies yield $^{40}Ar/^{39}Ar$ ages between 55.7 and 38.5 Ma and show that gold mineralization is the youngest among the different dated events. This Eocene age is consistent with the young structural setting of the gold orebodies revealing an emplacement along northwest-oriented normal faults, which can be correlated with Tertiary extensional tectonic events reported by previous field investigations. The data also indicate that gold ore formation is coeval with magmatism in the adjacent Tertiary Urumieh-Dokhtar magmatic belt and with intrusive activity within the Sanandaj-Sirjan zone, with a $^{40}Ar/^{39}Ar$ age of 54 Ma near Muteh according to our study. The remaining $^{40}Ar/^{39}Ar$ data reveal a Cretaceous to early Tertiary metamorphic, magmatic, and deformation history of the complex hosting the Muteh gold deposit.

The fluid inclusion study showed that distinct fluids were present during the regional geologic evolution predating ore formation and later Eocene gold ore formation. Early regional fluids consist of an $H_2O-CO_2-NaCl$ fluid with subsidiary $N_2$ and $CH_4$ that underwent local unmixing. The salinities of the liquid-rich inclusions resulting from unmixing range between 2.2 and 17.5 wt percent NaCl equiv, and those of the $CO_2$-rich, vapor-rich inclusions range between 2.8 and 7.2 wt percent NaCl equiv. The high salinity of the regional liquid-rich fluids is attributed to metamorphism of evaporite-bearing sedimentary rocks, magmatic intrusions, retrograde hydration reactions, metamorphism of impure marbles, and migmatization. The fluid inclusions spatially associated with the gold veins postdating regional metamorphism and ductile deformation of the host rocks contain a low-salinity aqueous fluid with a dilute, low-density $CO_2$ component, and maximum salinities between 2.6 and 5.8 wt percent NaCl equiv.

Gold deposition at Muteh occurred during or after late stages of Eocene brittle extension as a result of exhumation of the host metamorphic complex, possibly during magmatic activity in the Sanandaj-Sirjam zone. It is most likely linked to the introduction of a distinct low-salinity, low $CO_2$ content aqueous fluid during crustal extension. These fluids are younger than, and therefore unrelated to, the highly saline and $CO_2$-rich, regional metamorphic-magmatic fluids. Our results refute previous models advocating Precambrian to Paleozoic ages of the Muteh gold deposit.

[†] Corresponding author: e-mail, Robert.Moritz@terre.unige.ch

## Introduction

THE NORTHWEST-TRENDING Zagros orogen resulted from Cretaceous and Tertiary convergence between the Eurasian and the Afro-Arabian plates and constitutes a link between the European Alpine and the Pacific systems of the Tethyan Eurasian metallogenic belt (Jankovic, 1977, 1997). The Zagros orogen is subdivided into three parallel belts including, from northeast to southwest (Fig. 1), the Tertiary Urumieh-Dokhtar magmatic belt (Schröder, 1944; Förster, 1978; Berberian and Berberian, 1981), the Sanandaj-Sirjan tectonic zone (Mohajjel and Ferguson, 2000; Mohajjel et al., 2003; Agard et al., 2005), and the Zagros fold belt (Stöcklin, 1968; Mohajjel et al., 2003). The geodynamic and metallogenic setting of the Tertiary Urumieh-Dokhtar magmatic belt and its ore deposits, including porphyry copper and skarn deposits (Bazin and Hübner, 1969a, b; Waterman and Hamilton, 1975; Hezarkhani and Williams-Jones, 1998; Karimzadeh Somarin and Moayyed, 2002), is explained within a typical subduction context (Förster, 1974, 1978). By contrast, our knowledge of ore deposits in the adjacent Sanandaj-Sirjan zone, and their geodynamic and metallogenic setting, remains unsatisfactory. The relationship of ore deposits from this tectonic zone with the geologic evolution of the Zagros orogen is poorly constrained to unknown. This is a consequence of the fact that the Sanandaj-Sirjan zone is the result of a complex protracted Late Precambrian to Tertiary evolution, accompanied by multiple deformation events and local greenschist to amphibolite facies metamorphism.

This contribution is aimed at improving our knowledge of the metallogeny of the Sanandaj-Sirjan tectonic zone and is based on new field and analytical data gathered on the Muteh gold deposit, a major Iranian gold mine (Farhangi, 1991) hosted by metamorphic rocks of the Sanandaj-Sirjan zone, about 240 km southwest of Tehran in the Esfahan province (Fig. 1). Early studies have interpreted the metamorphic host rocks as Precambrian in age and as the eastern extension of the Proterozoic Arabian Shield (Thiele, 1966; Stöcklin, 1968, 1974; Thiele et al., 1968), and a Precambrian to early Paleozoic age was favored for the Muteh gold deposit. Various genetic interpretations have been suggested, including a metamorphogenic origin (Paidar-Saravi, 1989), a relationship to granitic intrusions of assumed Precambrian age (Thiele et al., 1968; Samani, 1988), and an exhalative hot-spring origin related to Paleozoic rhyolitic-acidic tuffs (Rachidnejad-Omran et al., 2002). Samani (1988) correlated the Muteh gold deposit with Proterozoic auriferous quartz veins in Egypt and Arabia. These relatively old ages and genetic relationships are suspect because most of the geologic evolution of the Andean-type Sanandaj-Sirjan zone is related to the Cretaceous to Tertiary closure of the Tethys (Mohajjel et al., 2003; Agard et al., 2005; Ghasemi and Talbot, 2006), accompanied by Late Jurassic to Eocene calc-alkaline magmatism (Förster, 1974; Berberian and Berberian, 1981; Berberian and King, 1981; Berberian et al., 1982; Braud, 1987; Agard et al., 2005; Ghasemi and Talbot, 2006), and that a majority of the metamorphic rocks of the Sanandaj-Sirjan zone are, in fact, metamorphosed equivalents of Paleozoic and Mesozoic units (Berberian and King, 1981; Davoudzadeh et al., 1986; Braud, 1987; Davoudzadeh and Weber-Diefenbach, 1987; Rachidnejad-Omran et al., 2002; Mohajjel et al., 2003; Sheikholeslami et al., 2003; Baharifar et al., 2004).

In order to understand the paradoxical setting of a reputedly old deposit of Late Precambrian to Paleozoic age within a younger Mesozoic to Tertiary orogen, we examined the relative age relationships between gold ore-controlling structures, related hydrothermal alteration, host-rock structures, and metamorphic mineral assemblages and present new $^{40}Ar/^{39}Ar$ data from biotite and amphibole in metamorphic and magmatic rocks within the gold district, and on muscovite from the gold veins and associated hydrothermal alteration. Fluid inclusion microthermometry and Raman spectroscopy were carried out to identify the ore-related fluid and to compare this to regional fluids that were present in the metamorphic host-rock complex. These data are discussed in the context of regional geologic studies and recent geodynamic syntheses by Mohajjel et al. (2003), Agard et al. (2005), and Ghasemi and Talbot (2006), and previous genetic models for the Muteh deposit are reassessed.

## Regional Geology

The development of the 1,500-km-long, 150- to 200-km-wide, Sanandaj-Sirjan zone (Fig. 1A) was related to the generation of the Tethys ocean and its subsequent destruction during Cretaceous and Tertiary convergence and continental collision between the Afro-Arabian and the Eurasian plates (Mohajjel et al., 2003; Agard et al., 2005; Ghasemi and Talbot, 2006). The predominantly Mesozoic and Tertiary marine and continental sedimentary sequences and the major unconformities and the structural framework of the Sanandaj-Sirjan zone are comparable to those of the Central Iranian block in the east. Therefore, post-Permian rocks of the Sanandaj-Sirjan zone are considered as having a Eurasian affinity by most authors (Stöcklin, 1968; Berberian and King, 1981; Braud, 1987; Davoudzadeh and Weber-Diefenbach, 1987; Hooper et al., 1994; Mohajjel et al., 2003; Agard et al., 2005), except Alavi (1994) who favors an Arabian affinity. Late Jurassic to Tertiary Alpine compressive tectonic events have imparted the characteristic structural trend to the Sanandaj-Sirjan zone, with northwest-oriented parallel belts of sedimentary and metamorphic rocks (Fig. 1B), northwest-trending folds partly overturned to the south and southwest, southwest-verging thrusts, and northwest-trending high-angle reverse faults, which resulted in thickening of the crust and Tertiary uplift of the Sanandaj-Sirjan zone (Stöcklin, 1968; Braud and Ricou, 1971; Berberian and King, 1981; Mohajjel and Fergusson, 2000; Mohajjel et al., 2003; Agard et al., 2005; Ghasemi and Talbot, 2006).

Late Jurassic to Eocene calc-alkaline magmatism of the Sanandaj-Sirjan zone, with peak activity during Late Cretaceous (Berberian and Berberian, 1981), is linked to northeastward subduction underneath Central Iran (Förster, 1974; Berberian and Berberian, 1981; Berberian and King, 1981; Berberian et al., 1982; Braud, 1987; Agard et al., 2005; Ghasemi and Talbot, 2006). Tertiary calc-alkaline magmatism in the adjacent Urumieh-Dokhtar magmatic belt (Fig. 1A; Förster, 1974; Berberian and Berberian, 1981; Berberian and King, 1981; Berberian et al., 1982) is interpreted by Ghasemi and Talbot (2006) to have resulted from slab breakoff during
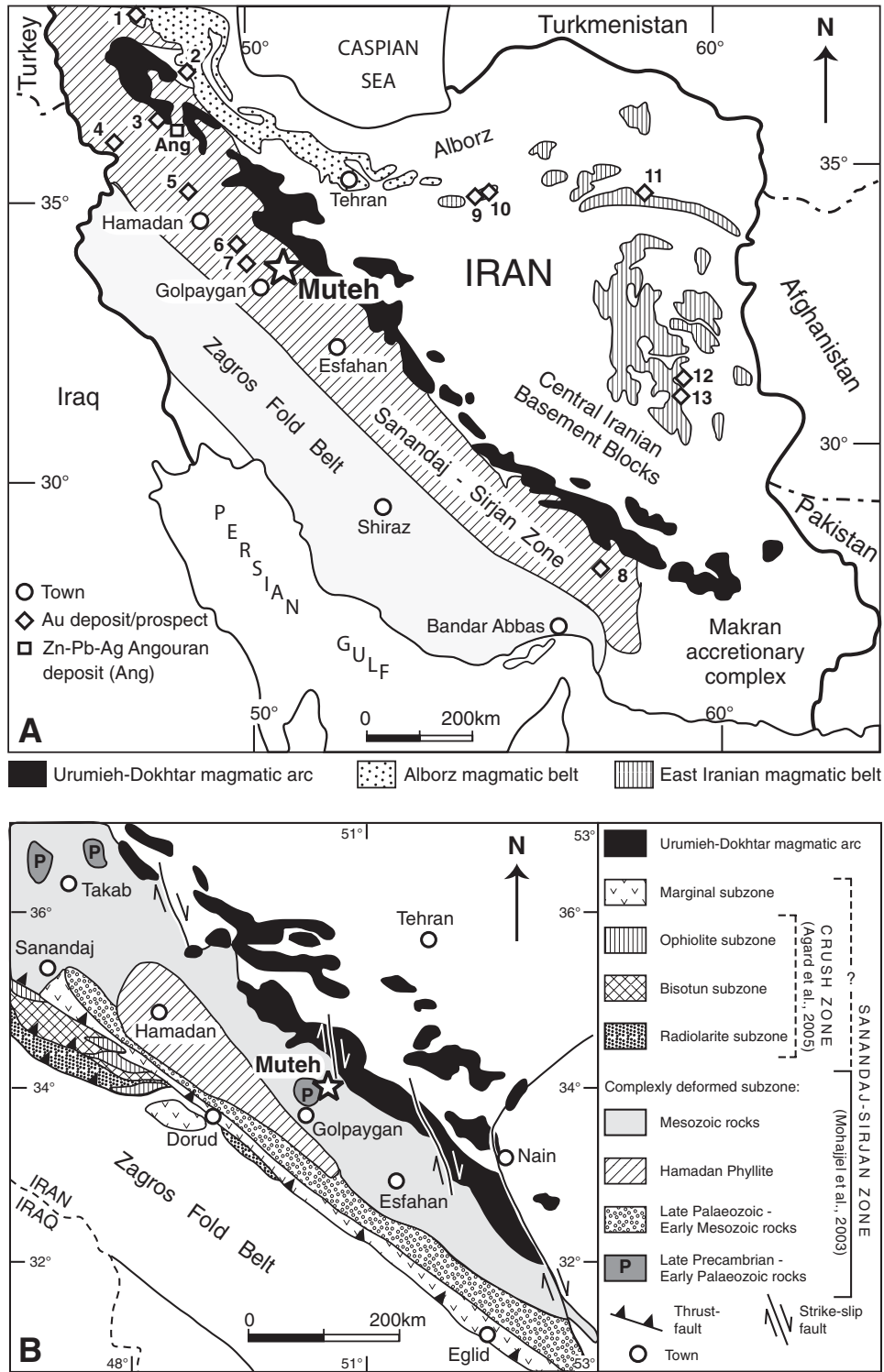
FIG. 1. A. Main tectonic elements and Mesozoic-Cenozoic magmatic belts of Iran (after Stöcklin, 1968, and Alavi et al., 1997) and location of gold occurrences, prospects, and mines in Iran: 1 = Kharvana, 2 = Mianeh, 3 = Zarshuran-Agh Darreh, 4 = Kervian, 5 = Dashkasan-Baharlu, 6 = Ahangaran, 7 = Astaneh, 8 = Zartorosht, 9 = Gandy-Abolhassani, 10 = Kuh-e Zar, 11 = Chelpow, 12 = Qal'eh Zari, 13 = Shalir (locations are from Lescuyer et al., 2003, except location 4 from Heidari et al., 2006, locations 6–8 from www.gsi.ir, and location 9 from Shamanian et al., 2004). Ang = Miocene Angouran Zn-Pb-Ag deposit linked to metamorphic core complex exhumation in the Sanandaj-Sirjan zone (Gilg et al., 2006). B. Simplified tectonic map of southwestern Iran, showing the subdivisions of the Sanandaj-Sirjan tectonic zone. There is still a matter of debate about the attribution of the Ophiolite, Bisotun, and Radiolarite subzones; Mohajjel et al. (2003) include them in the Sanandaj-Sirjan tectonic zone, whereas Agard et al. (2005) group them in a separate zone of Arabian affinity termed the Crush zone.

the middle Eocene. Agard et al. (2005) also suggested slab detachment, but only during a short interval during the late Eocene (40–38 Ma), based on K-Ar ages of mafic intrusions emplaced within the Sanandaj-Sirjan zone, 200 km northwest of Muteh (Leterrier, 1985; Braud, 1987). Older magmatic activity in the Sanandaj-Sirjan zone includes Late Triassic and Early Jurassic tholeiitic mafic volcanic rocks (Alavi and Mahdavi, 1994), interpreted as remnants of Tethyan oceanic crust (Mohajjel et al., 2003), and Late Proterozoic to early Paleozoic mafic rocks formed during extensional events (Berberian and King, 1981; Rachidnejad-Omran et al., 2002).

The complexly deformed subzone of the Sanandaj-Sirjan zone, which hosts the Muteh gold deposit (Fig. 1B), is characterized by abundant greenschist and amphibolite facies metamorphic rocks (Mohajjel et al., 2003), and recent investigations have revealed that a majority of them are metamorphosed equivalents of partly fossiliferous Paleozoic and Mesozoic units (Davoudzadeh et al., 1986; Braud, 1987; Davoudzadeh and Weber-Diefenbach, 1987; Rachidnejad-Omran et al., 2002; Mohajjel et al., 2003; Sheikholeslami et al., 2003; Baharifar et al., 2004). Therefore, reports of Hercynian (e.g., Thiele et al., 1968; Berberian and Berberian, 1981; Berberian and King, 1981) and older orogenies are disputed by many authors (Stöcklin, 1968; Crawford, 1977; Alavi, 1994; Rachidnejad-Omran et al., 2002), and much of the deformation, metamorphic and magmatic events in the Sanandaj-Sirjan zone are related to the closure of the Tethys ocean (Mohajjel et al., 2003). An extensive period of Middle Jurassic to Late Cretaceous medium- and high-pressure metamorphism was attributed by Berberian and King (1981) to orogenic events during subduction of oceanic crust beneath the Sanandaj-Sirjan zone. Regional low pressure and contact metamorphism, with andalusite, sillimanite, cordierite, and garnet, is mainly associated with and preceded the emplacement of Late Cretaceous granitic intrusions in the Sanandaj-Sirjan zone (Berberian and Berberian, 1981; Braud, 1987; Baharifar et al., 2004).

## Local Geologic Setting

Mesozoic and Tertiary sedimentary rocks overlying Paleozoic sedimentary rocks predominate in the study area and are largely covered by Quaternary rocks. Subsidiary Eocene volcanic rocks of the Urumieh-Dokhtar magmatic belt occur in the northeastern part (Fig. 2; Thiele et al., 1968). Metamorphic rocks of the Sanandaj-Sirjan zone in the Muteh area consist of gneiss, marble, amphibolite, mica schist, phyllite, quartzite, decimeter-thick to several-meters-long quartz veins, and rare meter-thick magnetite-rich horizons (Thiele et al., 1968).

Thiele (1966) and Thiele et al. (1968) assigned a Precambrian age to the metamorphic rocks, based on the assumption that overlying unmetamorphosed rock formations were Late Precambrian, Infracambrian, and Cambrian (see legend of Fig. 2: so-called Soltanieh, Zaigun-Lalun, Mila, Kahar, and Precambrian formations according to Thiele et al., 1968). Using new paleontological evidence, Rachidnejad-Omran et al. (2002) revised the stratigraphic column and suggested younger ages for the pre-Permian rock formations (Fig. 2), although they do not exclude the presence of Late Proterozoic rocks in the metamorphic complexes. According to this study,

unmetamorphosed dolomite, sandstone, and shale bordering the metamorphic complexes are Early Carboniferous and Devonian in age rather than Cambrian and Precambrian, respectively, and the metamorphic rocks consisting of gneiss, marble, amphibolite, schist, phyllite, and quartzite are interpreted as Cambrian instead of Precambrian (see legend describing the Sanandaj-Sirjan zone rocks in Fig. 2).

The western metamorphic complex, immediately to the northeast of the town of Golpaygan (Fig. 2), reached amphibolite facies conditions (Thiele, 1966). It is dominated by a kyanite-sillimanite-staurolite-biotite-garnet-plagioclase-ilmenite ± muscovite assemblage, typical of metamorphosed pelites, locally interlayered with marble. Tourmaline and scapolite were recognized during our study as subordinate phases in the metamorphosed pelites and marble, respectively. Rachidnejad-Omran et al. (2002) also mentioned the presence of small bodies of migmatite in gneiss of the western metamorphic complex. Based on our observations, the metamorphic assemblage is partly retrograde, as garnet is replaced by chlorite, muscovite, and staurolite, staurolite is replaced by chlorite and muscovite, and sillimanite is transformed into kyanite. The eastern metamorphic complex, which hosts the Muteh gold deposit (Fig. 2), is greenschist grade (Paidar-Saravi, 1989), with an assemblage predominantly composed of albite-chlorite-muscovite-biotite-quartz ± epidote, which overprints the amphibolite assemblage according to Thiele (1966) and Thiele et al. (1968).

Small dioritic to gabbro-dioritic plugs intruding Late Cretaceous marl and shale formations have been interpreted by Thiele et al. (1968) as hypabyssal expressions of Early Tertiary magmatism and are possibly equivalents of gabbro-diorite plugs in the Sanandaj-Sirjan zone about 200 km northwest of Muteh, which yielded K-Ar ages of 34 and 40 Ma, (Leterrier, 1985; Braud, 1987). Medium-grained biotite and two-mica granodiorite and granite intrusions were emplaced in Late Triassic (Rachidnejad-Omran et al., 2002) and Early Jurassic sedimentary rock formations (Thiele et al., 1968). Pebbles of such granitic intrusions were observed in Middle Cretaceous basal conglomerates by Thiele et al. (1968) and were interpreted as Late Jurassic to Early Cretaceous by the later authors. Similar granitic and dioritic intrusions were emplaced in the metamorphic complex hosting the Muteh gold deposit (Fig. 2). Thiele et al. (1968) assigned a Late Precambrian age to these intrusions, based on the observations that those intruding metamorphic rocks are more deformed than those hosted by Jurassic sedimentary rocks, and that the intrusions did not cut overlying dolomite, interpreted as Infracambrian (Fig. 2; i.e., the dolomite now interpreted as lower Carboniferous by Rachidnejad-Omran et al., 2002). Rachidnejad-Omran et al. (2002) obtained whole-rock and biotite K-Ar ages between 57.1 ± 1.8 and 64.2 ± 2.4 Ma for granite and a diorite emplaced in the metamorphic complex north of the town of Golpaygan (Fig. 2) and, therefore, proposed a Paleocene age for these intrusions.

## Gold Metallogeny of Iran

Iran's gold production is modest (ca. 600 kg/yr), and the gold deposits and prospects recognized so far are rather small in size, with only a few of them having been studied and described. The gold potential of Iran still remains to be fully
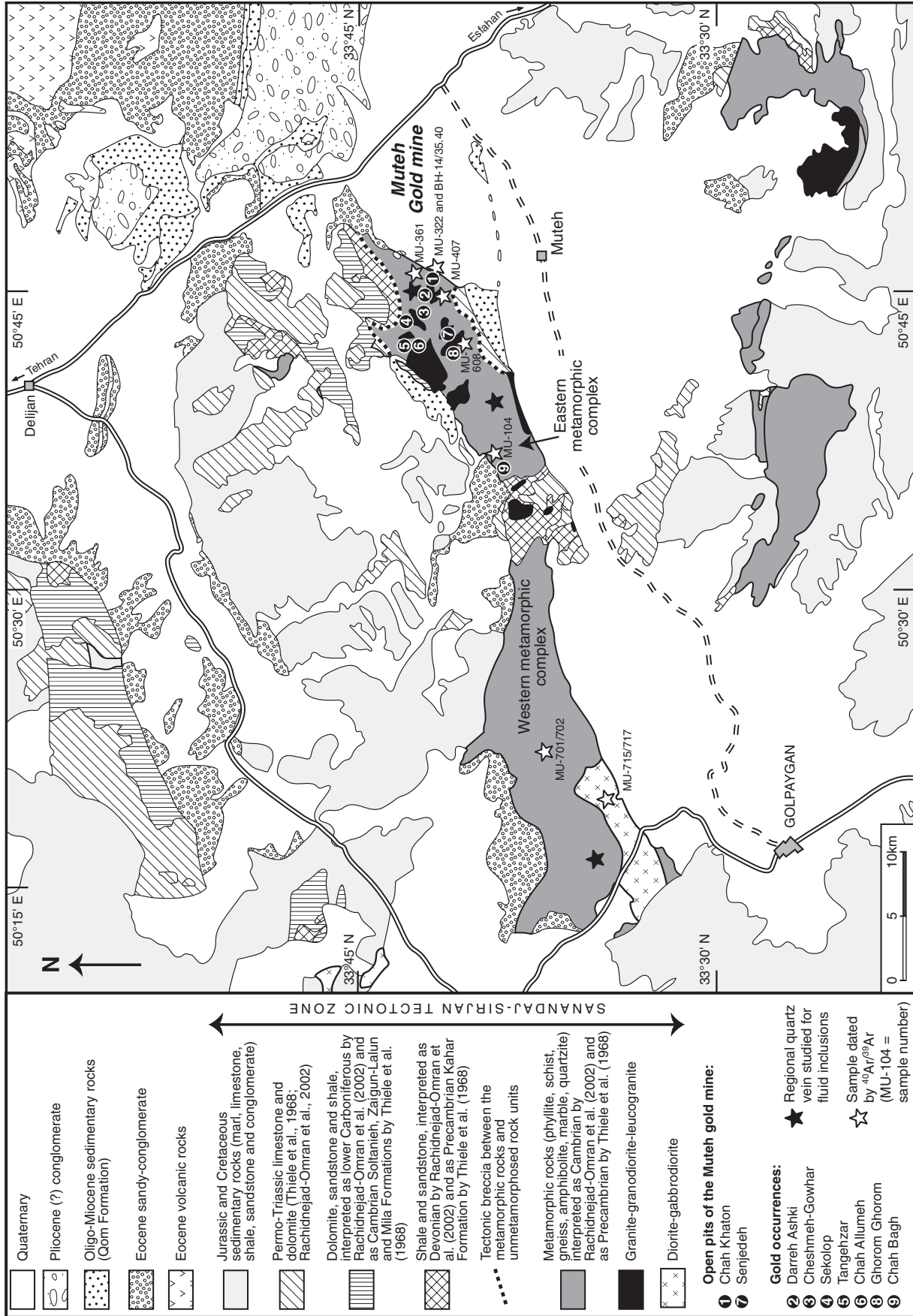
FIG. 2. Simplified geologic map of the Muteh-Golpaygan area (after Thiele et al., 1968, and updated according to Rachidnejad-Omran et al., 2002). Open pit and ore zone locations are from unpublished maps of the Iranian Mining and Metallurgy Company.

assessed (Lescuyer et al., 2003). A majority of the gold deposits and prospects are epithermal and are located within the Tertiary Urumieh-Dokhtar, Alborz, and East Iranian magmatic belts (locs. 1–3 and 9–13, Fig. 1A). They include the recently described Miocene sedimentary rock-hosted, gold-arsenic Zarshuran, Carlin-type deposit, Azarbaidjan province, northwest Iran, with 2.5 million metric tons (Mt) at 10 g/t of gold (Mehrabi et al., 1999; Asadi et al., 2000; loc. 3, Fig. 1A), and the volcanic rock-hosted Gandy and Abolhassani prospects in the Alborz magmatic arc, Semnan province (Shamanian et al., 2004; loc. 9, Fig. 1A). Further potential gold resources in the Tertiary magmatic belts are related to iron oxide copper-gold and porphyry-copper deposits (Lescuyer et al., 2003).

Except for the Muteh gold deposit, only minor gold occurrences have been recognized so far in the Sanandaj-Sirjan zone, including Kervian (Heidari et al., 2006), Ahangaran, Astaneh, and Zartorosht (locs. 4, 6–8, Fig. 1A). The gold-antimony-arsenic Dashkasan-Baharlu epithermal occurrence, Kordestan province (loc. 5, Fig. 1A) with 14 Mt at a gold grade of 1.9 g/t (Geological Survey or Iran, www.gsi.ir) is located in the Sanandaj-Sirjan zone, but it belongs to a Tertiary event, as it is hosted by Miocene dacite domes crosscutting Mesozoic sedimentary rocks (Lescuyer et al., 2003).

## The Muteh Gold Deposit

The Muteh gold mine lies between 1,800 and 2,200 m asl in the eastern part of the main northeast-elongated metamorphic complex north of the village of Muteh (Fig. 2). There are numerous old vertical surface diggings in the area, which are attributed to gold mining during the Sassanian and the Islamic periods (3rd-11th centuries) and which led to the rediscovery of the Muteh gold mine (Wertime, 1968). Initial exploration took place between 1955 and 1966 and was followed between 1980 and 1985 by detailed geologic studies, geochemical and geophysical surveys, and drilling. The Iranian Mining and Metallurgy Company determined average ore grades of 4 to 5 g/t (Paidar-Saravi, 1989; Farhangi, 1991). Presently, the Muteh gold mine consists of two main ore zones, including the Chah Khaton and Senjedeh open pits, and seven smaller occurrences (Fig. 2). Internal mine reports indicate a total tonnage (including remaining resources and past production) of 1.79 Mt at a grade of 2.85 g/t at Chah Khaton and of 1.76 Mt at a grade of 2.57 g/t at Senjedeh. The production was about 300 kg of gold in 2004 according to the Geological Survey of Iran (www.ngdir.com/plants/). The ore consists of nonrefractory oxide (0.38 Mt at a grade of 3.31 g/t at Chah Khaton and 0.84 Mt at a grade of 2.61 g/t at Senjedeh) and refractory sulfide (1.41 Mt at a grade of 2.73 g/t at Chah Khaton and 0.92 Mt at a grade of 2.54 g/t at Senjedeh). The oxide ore was exhausted in 2000.

### Host rocks

The rocks in the vicinity of the Muteh deposit are predominantly schist and gneiss, subsidiary amphibolite and quartzite, and local marble and magnetite horizons (Thiele et al., 1968; Paidar-Saravi, 1989). The schist contains mainly quartz, biotite, chlorite, and muscovite. Paidar-Saravi (1989) subdivided the schist into different varieties, based on the predominant phases (e.g., mica, quartz-muscovite, quartz-chlorite, quartz-biotite-chlorite, and chlorite-biotite schist). However, the contacts among the different schist types and gneiss are diffuse or gradational, and this explains why no individual, persistent lithologic units were mapped across the entire eastern metamorphic complex by Paidar-Saravi (1989). Thiele et al. (1968) interpreted the gneiss as a metamorphosed equivalent of graywacke and quartzite.

The granitic rocks emplaced in the metamorphic complex in the immediate vicinity of the Muteh gold mine are medium-grained biotite and two-mica leucogranites, which locally can be extremely rich in quartz and feldspar and mica poor (Thiele et al., 1968). Hornfelsic rocks result from contact with the granite (Paidar-Saravi, 1989). The $SiO_2$ content of the granite varies between 75 and 81 wt percent (Paidar-Saravi, 1989; Rachidnejad-Omran et al., 2002; R. Moritz, unpub. data).

Paidar-Saravi (1989) also described a range of different metavolcanic rocks, including rhyolitic, dacitic, and andesitic tuff and lava, which were already described in internal reports of the Geological Survey of Iran (Momenzadeh, 1979; Alavi-Tehrani, 1980, cited in Paidar-Saravi, 1989). According to Paidar-Saravi (1989), these rocks have a grano-lepidoblastic texture with quartz and feldspar forming a mosaic intergrowth and mica and chlorite defining the foliation (see below). Pyrite and locally larger crystals of feldspar are also mentioned. Paidar-Saravi (1989) described the metavolcanic rocks as interlayered with schist but provided no further textural evidence that they are tuffs or lavas. During our fieldwork, we did not recognize any primary textures, and these rocks cannot be distinguished from the other metamorphic rocks in the area. Therefore, we refer to them as gneiss or schist. Rachidnejad-Omran et al. (2002) also mentioned the presence of metarhyolite and metavolcanic tuff, in spatial association with higher gold grades, but with no additional evidence for this rock classification. They interpreted the metarhyolite together with the amphibolite as a bimodal volcanic suite and the host schist and gneiss as an early Paleozoic (to Late Proterozoic?) volcano-sedimentary complex.

### Host-rock structures

In the Muteh gold mine area, the metamorphic rocks display a subhorizontal mylonitic foliation (Figs. 3A, 4A) with a northeast-oriented stretching lineation within the plane of foliation (Fig. 3A). This indicates that the metamorphic rocks have experienced extension in a northeast-southwest direction and flattening in a subvertical direction. Locally the granitic intrusions also contain a subhorizontal foliation (Fig. 4B), and apophyses of the diorite intrusion in the western part of the northeast-elongated metamorphic complex are also affected by subhorizontal isoclinal folding and the flat-lying foliation (Fig. 4C). Therefore, the intrusions hosted by the metamorphic rocks were emplaced before the end of ductile deformation. Decimeter-thick and meter-long metamorphic quartz segregation veins and layers of biotite-chlorite schist are concordant with the subhorizontal foliation of the host metamorphic rocks and are boudinaged or crosscut and displaced by normal faults (Fig. 4D). The subhorizontal layering of schists and quartz segregation veins is attributed to the transposition of the host-rock units during subvertical flattening and formation of the mylonitic foliation.

In the vicinity of the Muteh gold deposit, the subhorizontal mylonitic foliation increases in intensity upward, toward the

A: Foliation and lineation in the metamorphic host rocks　　　B: Structural data from the Chah Khaton open pit
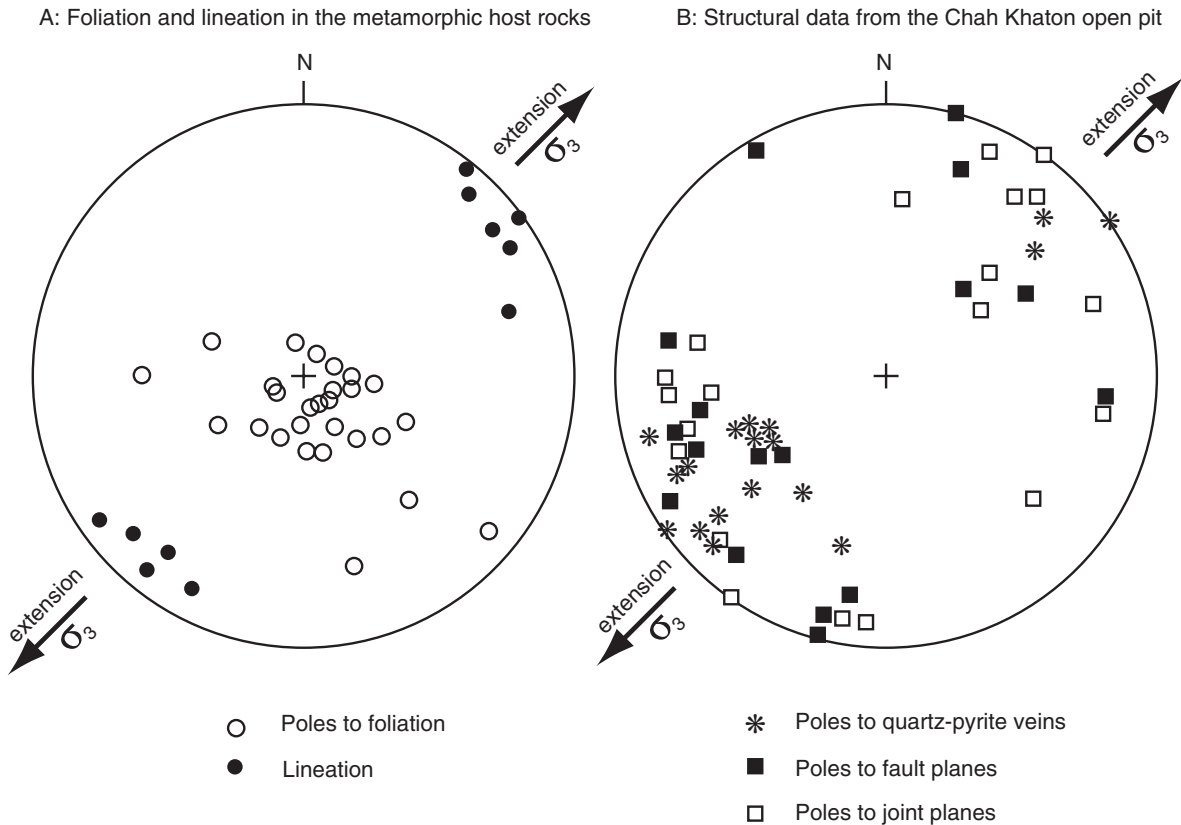


Fig. 3. Structural elements in the metamorphic host rocks and ore zones of the Chah Khaton and Senjedeh open pits, Muteh gold deposit. A. Host-rock structures at the Muteh gold mine with subhorizontal mylonitic foliation and northeast-oriented stretching lineation within the plane of the foliation. B. Structural data from the Chah Khaton open pit with north-west-striking normal faults, joints, and quartz-pyrite-carbonate veins displaying a conjugate system. Both the ductile and brittle structures of, respectively, the metamorphic host rocks and the ore zones indicate northeast-southwest extension and can be interpreted within a continuous ductile to brittle extensional evolution of the metamorphic complex at Muteh.

contact with the unmetamorphosed, Paleozoic sedimentary rocks. Immediately at this contact and structurally parallel to the mylonitic foliation of the metamorphic rocks is a thin horizon of microbreccia containing clasts of metamorphic rocks with a mylonitic fabric cemented by iron oxides (Fig. 4E-F). This breccia horizon can be traced along the contact with overlying younger, non- to slightly metamorphosed sedimentary rocks of various ages, including: pre-Permian shale, sandstone, and dolomite (interpreted as Cambrian-Precambrian by Thiele et al., 1968, and as Devonian-Early Carboniferous by Rachidnejad-Omran et al., 2002), Permian dolomite, and Tertiary sedimentary rocks (Fig. 2). Thus, there is a sharp contrast in deformation and metamorphic grade with an intense mylonitic fabric and a greenschist facies mineral assemblage in the metamorphic rocks beneath the breccia horizon and overlying essentially unmetamorphosed and nonpenetratively deformed sedimentary rocks.

The mylonite shows compositional layering where two quartz types can be recognized (Fig. 5): (1) fine-grained matrix quartz with approximately uniform grain sizes and irregular boundaries typical of dynamic recrystallization (Passchier and Trouw, 1998), and (2) coarser quartz grains arranged along bands forming the appendages (i.e., wings) attached to both sides of feldspar porphyroclasts. The larger quartz grains pass laterally into smaller, recrystallized new grains. The

quartz texture reflects a ductile behavior, whereas the broken feldspar porphyroclasts indicate a brittle behavior, thus revealing low to moderate degrees of deformation that may have occurred between about 350° and 600°C, according to Passchier and Trouw (1998, p. 52). Two foliation planes are defined by the preferential orientation of phyllosilicates (biotite, muscovite, chlorite) arranged in a C-S texture or C-type shear band texture (Fig. 5C). Kinematic indicators studied in thin sections cut parallel to the stretching lineation and normal to the foliation, collectively showing a subhorizontal shear sense for the mylonite with top to the northeast displacement (Fig. 5), which is opposite to the regional southwest-verging thrust geometry of the Sanandaj-Sirjan tectonic zone.

The silica-rich composition and the mineralogy of some parts of the mylonite including quartz, feldspar, muscovite, and biotite, which is partly to entirely replaced by chlorite, is indistinguishable from the leucogranites that intruded the metamorphic rocks in the Muteh gold mine area. In areas remote from the main open pits, such as at Ghorom Ghorom (see loc. 8, Fig. 2), one can recognize that the granitic intrusions are affected by the subhorizontal foliation (Fig. 4B). Therefore, we conclude that some of the more felsic subhorizontal mylonites recognized in the open pits at Chah Khaton and Senjedeh (see locs. 1 and 7, Fig. 2) are intensely deformed counterparts of the leucogranites, rather than rhyolitic
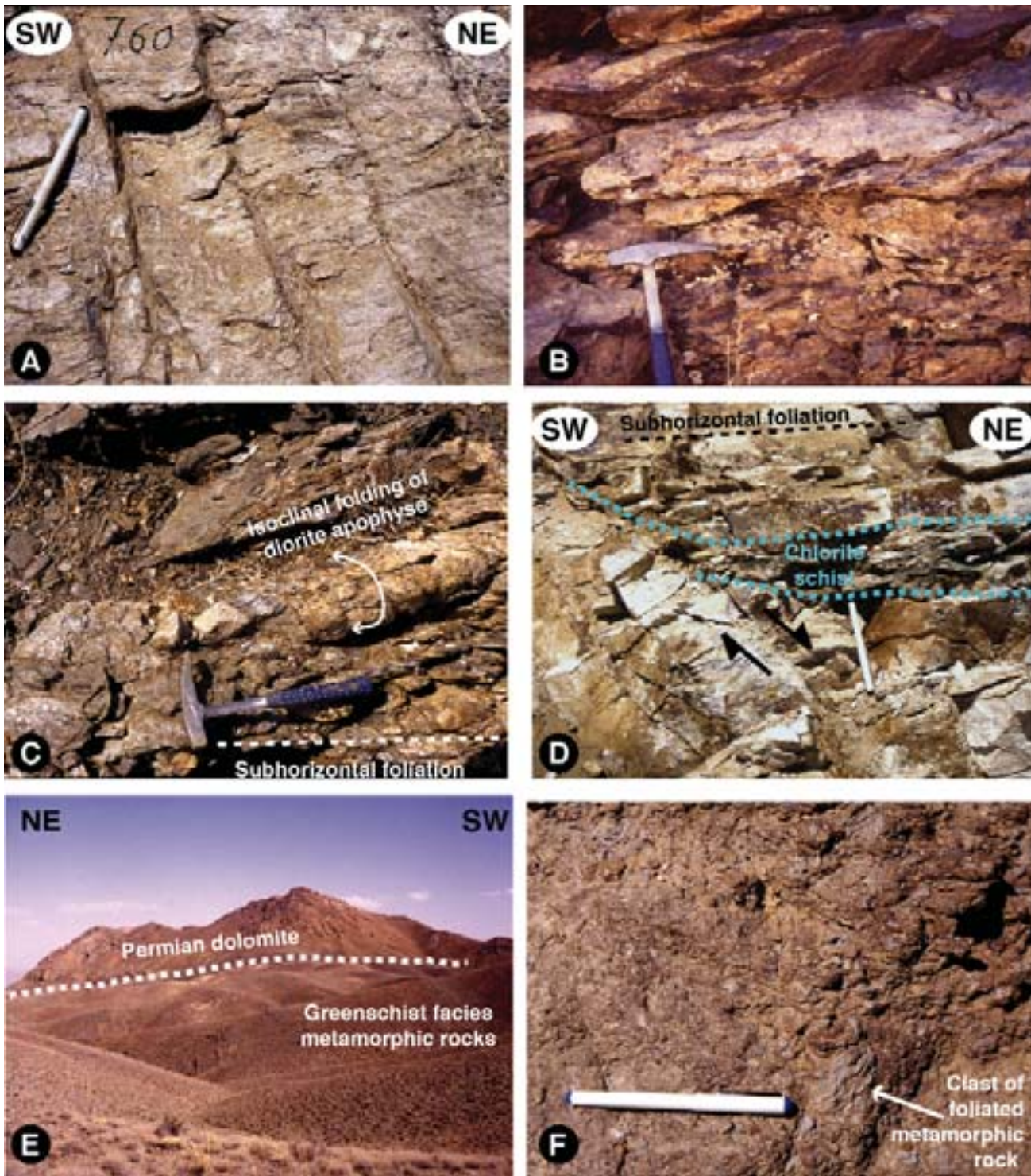
FIG. 4.  Structural elements in rocks from the Muteh gold mine area. A. Subhorizontal mylonitic foliation in the host rocks of the gold deposit. The foliation is crosscut by younger quartz-pyrite-carbonate veins belonging to the ore-forming event (Chah Khaton open pit, loc. 1, Fig. 2). B. Subhorizontal foliation affecting the leucogranite from the Muteh gold mine area (Ghorom Ghorom occurrence, loc. 8, Fig. 2). C. Subhorizontal isoclinal folding and foliation affecting the diorite intrusion in the western part of the metamorphic complex, north of the town of Golpaygan (Fig. 2). D. Flat-lying chlorite schist parallel to the subhorizontal mylonitic foliation of the host rocks in the Chah Khaton open pit. The chlorite schist has been crosscut by a younger normal fault. E. Subhorizontal, thin breccia horizon (white dotted line) between the greenschist facies metamorphic host rocks of the Muteh gold deposit and overlying Permian dolomite, immediately south of the Chah Khaton and Senjedeh open pits (Fig. 2). F. Close-up of the matrix-supported breccia horizon between the greenschist facies metamorphic rocks and the overlying unmetamorphosed sedimentary rocks. Clasts consist of metamorphic rocks with a mylonitic foliation and subsidiary quartz veins in a fine-grained, oxidized matrix.
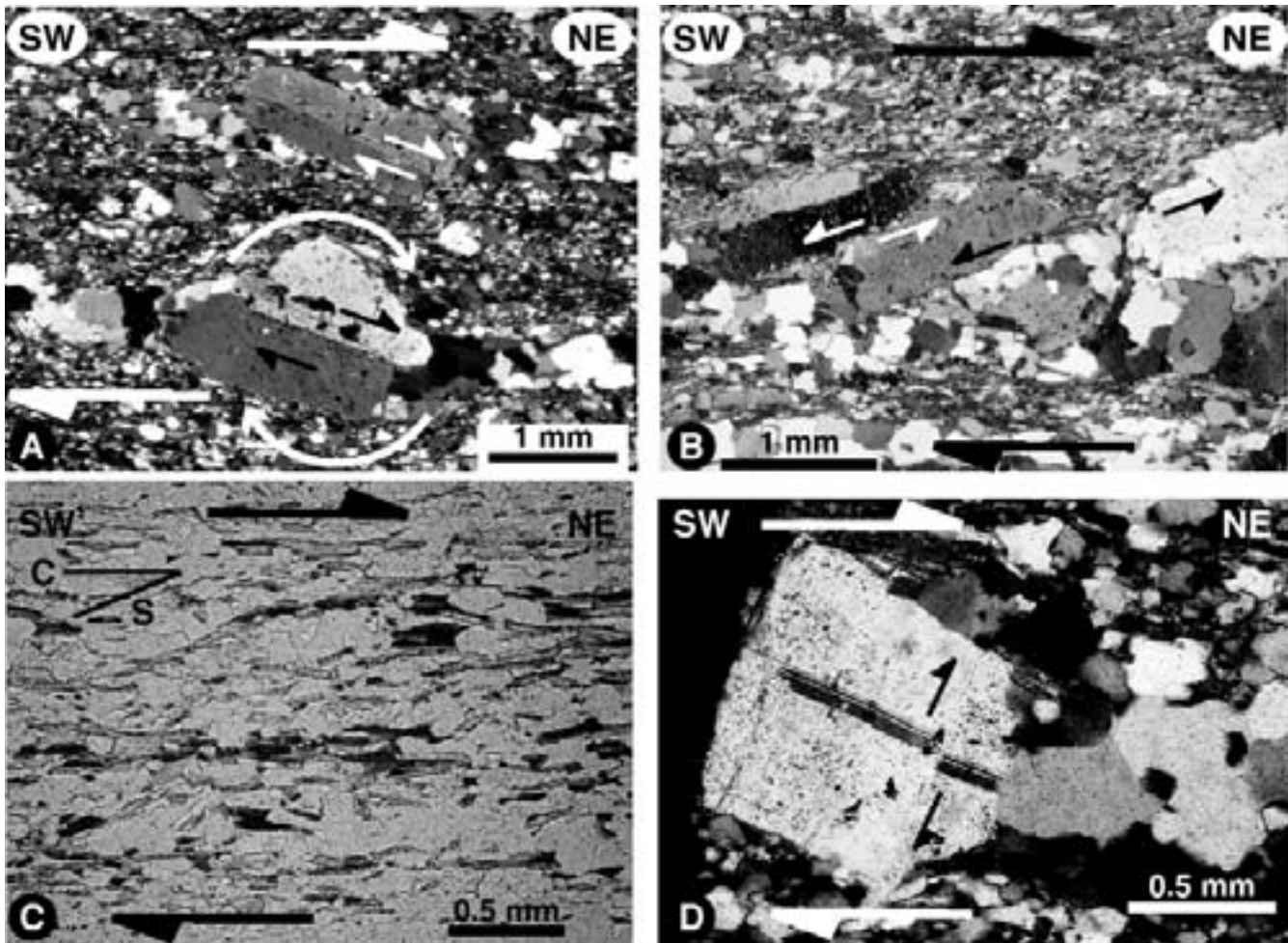
Fɪɢ. 5.  Microstructures in the subhorizontal mylonite at the Chah Khaton open pit (loc. 1, Fig. 2), showing a subhorizontal shear sense with top to the northeast displacement, opposite to the regional southwest-verging thrust within the Sanandaj-Sirjan tectonic zone. Sections are cut parallel to the stretching lineation and normal to the foliation plane. The sense of shear has been deduced according to criteria outlined in Passchier and Trouw (1998). A. Stepped, fragmented feldspar porphyroclasts with synthetic microfaults (Riedel fault) with respect to the main subhorizontal shear sense. The lower feldspar grain is a δ-type mantled porphyroclast with attached appendages of coarser quartz grains (i.e., wings), showing a clockwise rotation. B. Tiling imbrication of feldspar grains. C. C-type shear bands outlined by muscovite, biotite, and chlorite replacing biotite in the schist hosting the gold deposit. D. Synthetic microfault (thrust, P-type fault?) in a feldspar porphyroclast displacing twins of the host mineral.

metavolcanic rocks as suggested previously by Paidar-Saravi (1989) and Rachidnejad-Omran et al. (2002).

*Mineralization and wall-rock alteration*

Hydrothermal alteration associated with the gold occurrences is characterized by intense, pervasive bleaching of the host rocks. In areas where alteration is less intense, it can be seen that the bleaching occurs along small fractures crosscutting the subhorizontal foliation of the host rocks (Fig. 6A). It consists of silicified rock with microcrystalline to crystalline quartz, fine-grained muscovite, pyrite, dolomite-ankerite, and albite overprinting the metamorphic minerals of the host rocks (Figs. 6B, 7). Subsidiary alteration minerals are rutile and chlorite, replacing biotite. Irregular microscopic and straight macroscopic veining is also recognized with quartz, dolomite-ankerite, and pyrite as the dominant minerals, and subsidiary albite and muscovite. The veins crosscut the subhorizontal foliation of the host rocks (Fig. 4A). Breccias occur in places with fragments of silicified host rock cemented by late-stage carbonate. Thus, the textural, mineralogical, and vein relationships indicate that the gold mineralization postdated metamorphism and ductile deformation of the host rocks. Some of the quartz-carbonate-pyrite veins from the ore zones show open-space growth with euhedral quartz crystals arranged in a comb texture (Fig. 6C), which also supports a late timing of ore formation after ductile deformation of the host rocks. Hematite, kaolinite, and gypsum were formed during supergene alteration. It remains unclear whether the metarhyolite described by Rachidnejad-Omran et al. (2002) might correspond to the silica-rich and bleached rock characterizing the hydrothermal alteration, which is mapped by the local mine geologists as "metarhyolite," and which typically hosts the higher gold grades (A. Ghaedi and H. Reza-Feizi, Iran Gold Company, pers. commun., 1993).
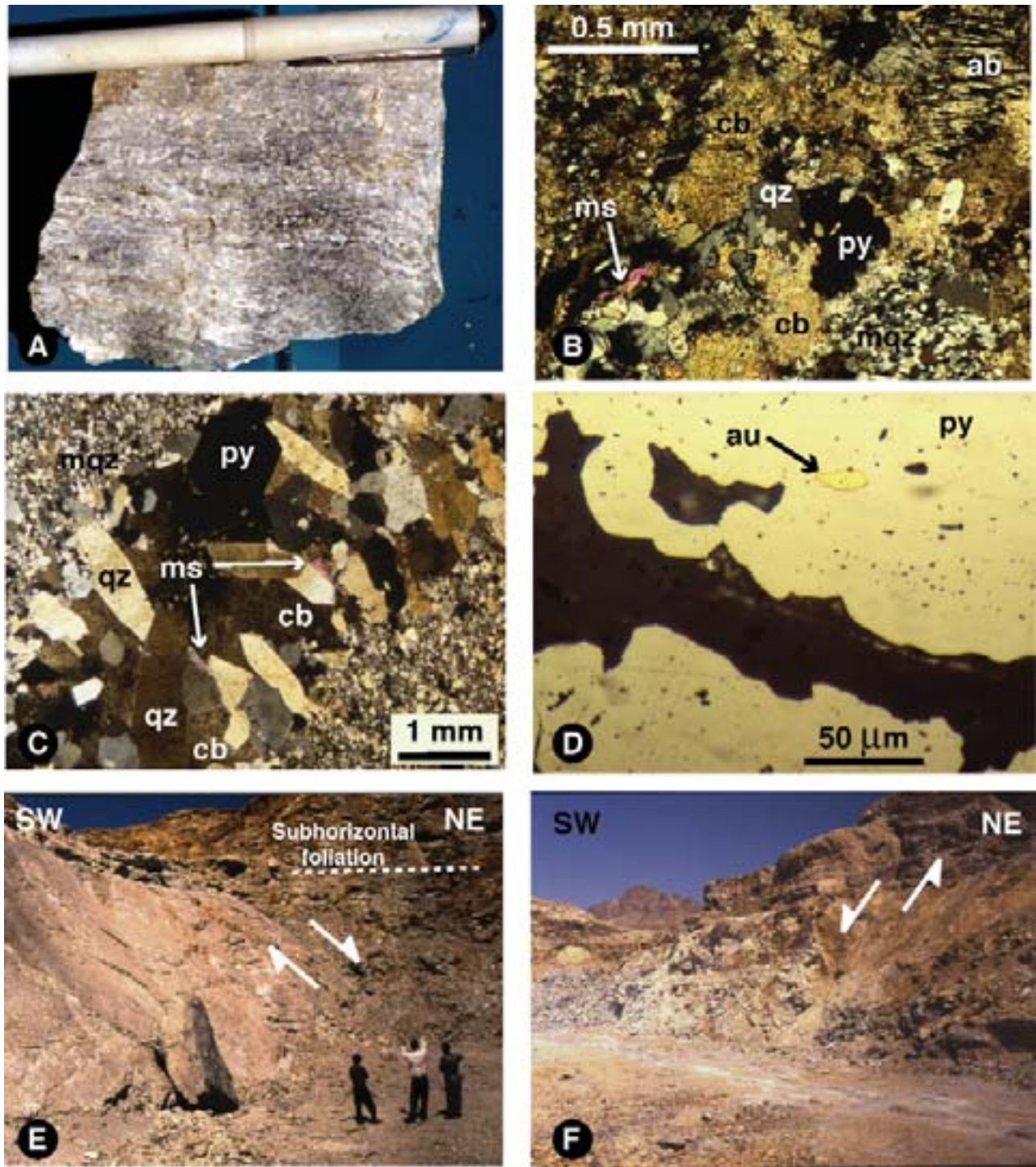
Fig. 6. A. Hydrothermal alteration bleaching the host rocks along small, subvertical quartz-pyrite veins crosscutting the subhorizontal foliation and the overprinting the metamorphic paragenesis of the host rocks. B. Hydrothermal alteration consisting of microcrystalline to crystalline quartz (mqz and qz, respectively), dolomite-ankerite (cb), pyrite (py), albite (ab), and muscovite (ms), crossed polars. C. Small quartz (qz)-carbonate (cb)-pyrite (py) vein containing hydrothermal muscovite (ms) emplaced in a silicified rock (mqz), crossed polars. The vein records open-space growth, with euhedral quartz crystals arranged in a comb texture. D. Gold inclusion (au) in pyrite (py), the predominant opaque mineral in the Muteh gold deposit (reflected, plane-polarized light). E. Southwestern extremity of the Chah Khaton open pit (loc. 1, Fig.2), showing a major northwestern-oriented and northeastern-dipping normal fault controlling the geometry of the gold orebodies. The normal fault crosscuts the subhorizontal foliation of the metamorphic host rocks. F. Northeastern extremity of the Chah Khaton open pit (loc. 1, Fig. 2), showing a major northwestern-oriented and southwestern-dipping normal fault controlling the geometry of the gold orebodies.

| | Least altered host rock | Alteration halo (bleached zone) | Vein |
|---|---|---|---|
| Quartz | ▬▬▬▬▬▬▬▬▬▬▬▬▬▬▬▬▬▬▬ | | |
| Plagioclase | ▬▬▬▬▬▬▬▬▬ | | |
| K-feldspar | ▬▬▬▬▬▬▬▬▬ | | |
| Biotite | ▬▬▬▬▬▬▬ | | |
| Muscovite | ▬▬▬▬▬▬▬▬▬▬▬▬▬▬▬▬▬▬▬ | | |
| Pyrite | ▬▬▬▬▬▬▬▬▬▬▬▬▬▬▬▬▬▬▬ | | |
| Rutile | | ▬▬▬▬▬▬▬▬▬▬▬▬▬ | |
| Albite | | ▬▬▬▬▬▬▬▬▬▬▬▬▬ | |
| Chlorite | | ▬▬▬▬▬▬▬▬▬▬▬▬▬ | |
| Carbonate | | ▬▬▬▬▬▬▬▬▬▬▬▬▬▬▬▬▬▬ | |

FIG. 7. Schematic alteration zonation profile around veins from the ore zones in felsic gneiss and granitic host rocks at Muteh.

Pyrite is the dominant opaque mineral and is the major phase associated with gold (Fig 6D). Chalcopyrite, marcasite, galenobismutite, bismuth, galena, sphalerite, and pyrrhotite are subsidiary to rare phases. Pyrrhotite was deposited early with pyrite, and the remaining opaque minerals, together with gold, postdate pyrite deposition, mostly along fractures. Chalcopyrite was deposited during both stages (Paidar-Saravi, 1989). Three types of pyrite have been observed during our study and include: (1) fine-grained, barren pyrite disseminated along the foliation of the host rocks; (2) pyrite aggregates in the host rocks or in metamorphic segregation quartz veins; and (3) coarse-grained, euhedral to subhedral pyrite in or immediately next to veins crosscutting the foliation of the host rocks (Fig. 4A). The later pyrite type is related to ore formation and is indicative of high gold grades (A. Ghaedi and H. Reza-Feizi, Iran Gold Company, pers. commun., 1993). Microprobe analyses by Paidar-Saravi (1989) showed that the Au/Ag ratio is about 8.5/1.

*Geometry and structural setting of the gold orebodies*

The structural elements associated with the orebodies were mainly studied on mine faces at the Chah Khaton and Senjedeh open pits (locs. 1 and 7, Fig. 2). The ore zone at Chah Khaton is within a conjugate fault system consisting of northwest-oriented normal faults dipping in opposite directions (Figs. 3B, 6E-F). In the ore zone, normal faults, joints, quartz-pyrite-carbonate veins, and a breccia zone have a northwest strike, also displaying a conjugate system, but with a preferential development of the brittle structures plunging to the northeast (Fig. 3B). The brittle structures crosscut the flat-lying ductile fabric of the host rock (Fig. 4A), and they record a northeast-southwest brittle extension parallel to the ductile fabric of the host rock. Drill core information shows that the zone with the highest gold grades and the associated alteration zone consisting of the highly bleached, siliceous

rocks at Chah Khaton also dip to the north and are discordant with respect to the subhorizontal layering of the host schists (Fig. 8). Thus, the geometry of the ore zone at Chah Khaton reveals a structural control of the gold mineralization by late brittle structures formed during extension and postdating the ductile deformation of the host rocks, including the granitic intrusions. The discordant relationship with respect to the host schists of the highly bleached, siliceous rocks defined as "metarhyolite" by the mine geologists (Fig. 8) indicates that they are a product of hydrothermal alteration along a crosscutting structure, rather than an original lithologic unit, such as a rhyolitic metavolcanic rock.

On a regional scale, the majority of the orebodies and ore occurrences are aligned along a northwestern trend (see alignment of ore zone locs. 1–6, Fig. 2), parallel to the orientation of faults, fractures, and veins recognized within the open pits of Chah Khaton and Senjedeh (Figs. 3B, 4A, 6E-F). The northwestern trend of the ore-controlling structures is recognized in most other ore occurrences of the Muteh gold mine area (Paidar-Saravi, 1989). Locally, a lithologic control of the ore occurrences can be recognized, such as gneiss-granite contacts at Ghorom Ghorom and Darreh Ashki (ore zone locs. 2 and 8, Fig. 2), and gneiss-amphibolite contacts at Chah Bagh (ore zone loc. 9, Fig. 2). Akin to our observations, Kouhestani (2005) and Kouhestani et al. (2005) stated that northwest-oriented normal faults plunging to the east host the mineralized zones at Chah Bagh. However, these authors also mentioned the presence of sulfide-bearing siliceous lenses parallel to the local subhorizontal mylonitic foliation at Chah Bagh (ore zone loc. 9, Fig. 2), which they interpret as evidence for the beginning of gold deposition during ductile deformation and before the onset of extensional brittle deformation.

### $^{40}Ar/^{39}Ar$ Geochronology

Previous dating has been carried out by Rachidnejad-Omran et al. (2002), using the conventional $^{40}K$-$^{40}Ar$ method. This technique is extremely useful for young undisturbed samples, but in many cases it is not adequate in terranes characterized by multiple stages of metamorphic, magmatic, deformation, and hydrothemal events, such as in the metamorphic complex at Muteh, which may result in partial argon loss or incorporation of excess argon (e.g., Hanes, 1991; Richards and Noble, 1998; Kelley, 2002). Under such conditions, the $^{40}K$-$^{40}Ar$ method commonly yields mixed and imprecise ages with no geologic significance. To overcome these problems, we have used the incremental-heating and in situ laser-ablation $^{40}Ar/^{39}Ar$ techniques to determine the age of gold mineralization and to constrain its timing with respect to the regional geologic evolution.

*Methodology*

$^{40}Ar/^{39}Ar$ experiments were undertaken by incremental heating on seven mineral separates and by in situ laser ablation on six polished whole-rock wafers to microsample (Kelley et al., 1994) from pure domains within small biotite, amphibole, and muscovite crystals. Mineral separates of amphibole, biotite, and muscovite were purified by crushing, sieving to 100 to 250 $\mu$m, and handpicking. Whole-rock wafers with a thickness of 1 mm were cut from 5-mm-diam drill cores. The mineral separates and the rock wafers were
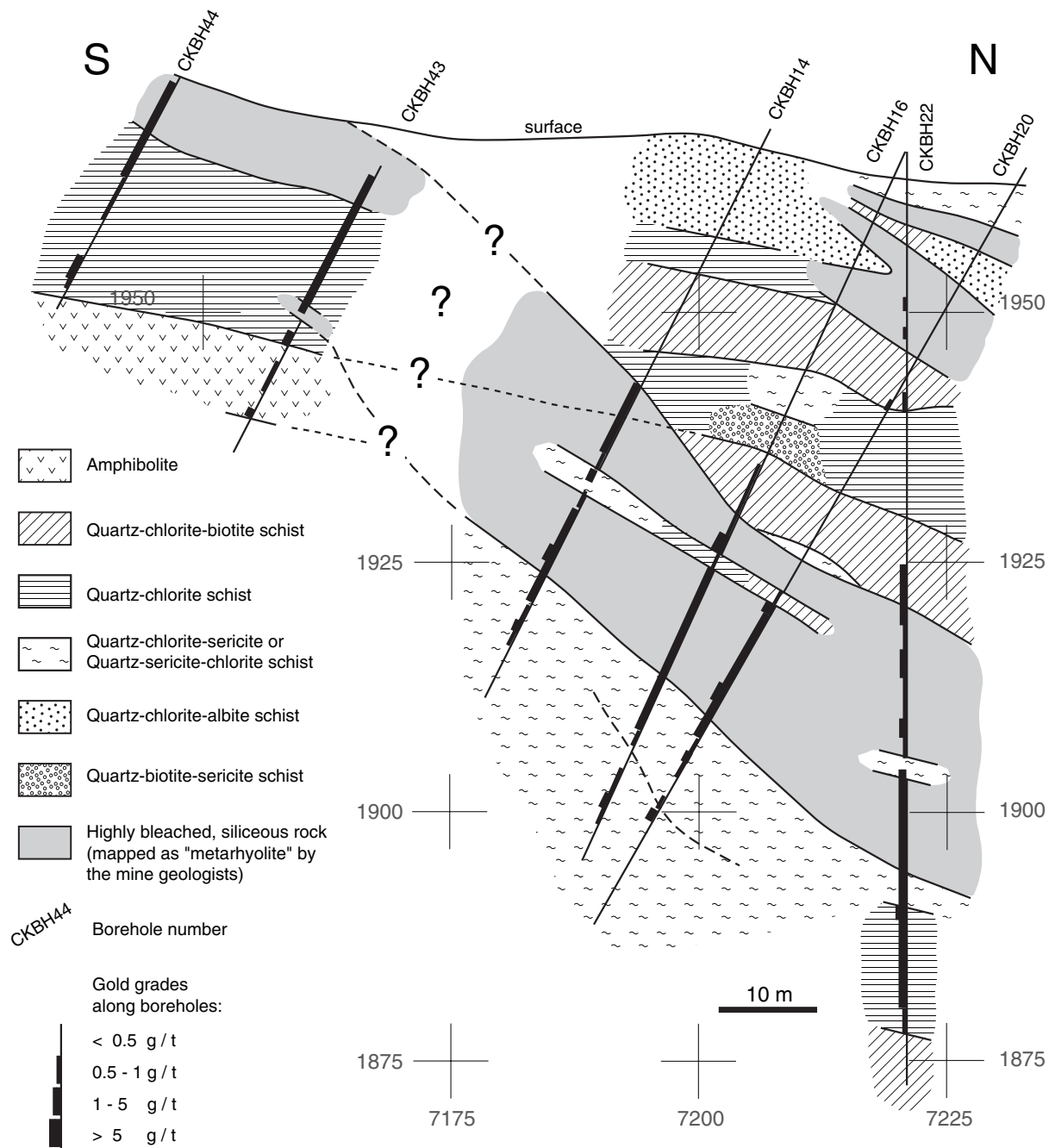
FIG. 8. North-south cross section, showing the discordant geometry of the highly bleached, siliceous rocks formed during hydrothermal alteration and gold ore formation compared to the subhorizontal layering of the metamorphic host rocks at the Chah Khaton open pit (loc. 1, Fig. 2). Drill core description and gold grades provided by the staff of the Muteh gold mine, Iranian Mining and Metallurgy Company.

wrapped in Al foil packets and encapsulated along with the neutron flux monitor into sealed quartz vials, which were irradiated at the Oregon State University Triga reactor. The neutron flux monitor was the 28.34 Ma sanidine from the Taylor Creek rhyolite (Renne et al., 1998). Details of analytical and data reduction procedures can be found in Singer and Pringle (1996) and Singer et al. (1999). Mineral separates were incrementally heated between approximately 360° and 1,250°C, in seven to 25 steps during 60 s each with a 25W

$CO_2$ laser with a faceted lens delivering a 9-mm² beam, evenly heating the sample. The amount of biotite and muscovite was between 0.2 and 0.3 mg, whereas 5 mg was used for amphibole. For in situ analyses of polished whole-rock wafers, the gas was extracted by ablation for 60 s using a 226-nm wavelength ultraviolet laser operated in a pulsed mode. Following 2 min of cleanup on SAES getters, isotope measurements of the gas were made in a MAP-216 spectrometer operated with a Bäur-Signer ion source and a Johnston electron

multiplier at the University of Geneva. Corrections for interfering reactions during irradiation of $^{40}K$ and $^{40}Ca$ were: $[^{40}Ar/^{39}Ar]_K = 0.00086$, $[^{36}Ar/^{37}Ar]_{Ca} = 0.000264$, and $[^{39}Ar/^{37}Ar]_{Ca} = 0.000673$. Ages were calculated using the decay constants of Steiger and Jäger (1977) and are reported with $\pm 2\sigma$ uncertainties. Inverse-variance weighted mean ages and errors were used for both the incremental-heating and in situ laser-ablation experiments.

## Results

*Regional metamorphic rock samples:* Incremental heating of a biotite from metapelite of the western metamorphic complex (MU-701, Fig. 2) yielded a strongly disturbed spectrum with a plateau segment at low percentages of $^{39}Ar$ released and a rising staircase pattern toward older apparent ages for higher released gas percentages (Fig. 9A). The plateau segment contained 61 percent of the total $^{39}Ar$ released and yielded an age of $108.29 \pm 0.92$ Ma. The last gas release with a significant $^{39}Ar$ content (third last step) yielded an apparent age of $129.69 \pm 2.86$ Ma (App. 1). In situ analyses of six single biotite crystals from the same locality and rock unit (MU-702, Fig. 2) yielded lower ages ranging between $63.7 \pm 3.8$ and $86.7 \pm 10.2$ Ma (Table 1, App. 2). Incremental heating experiments of mineral separates from an amphibo-
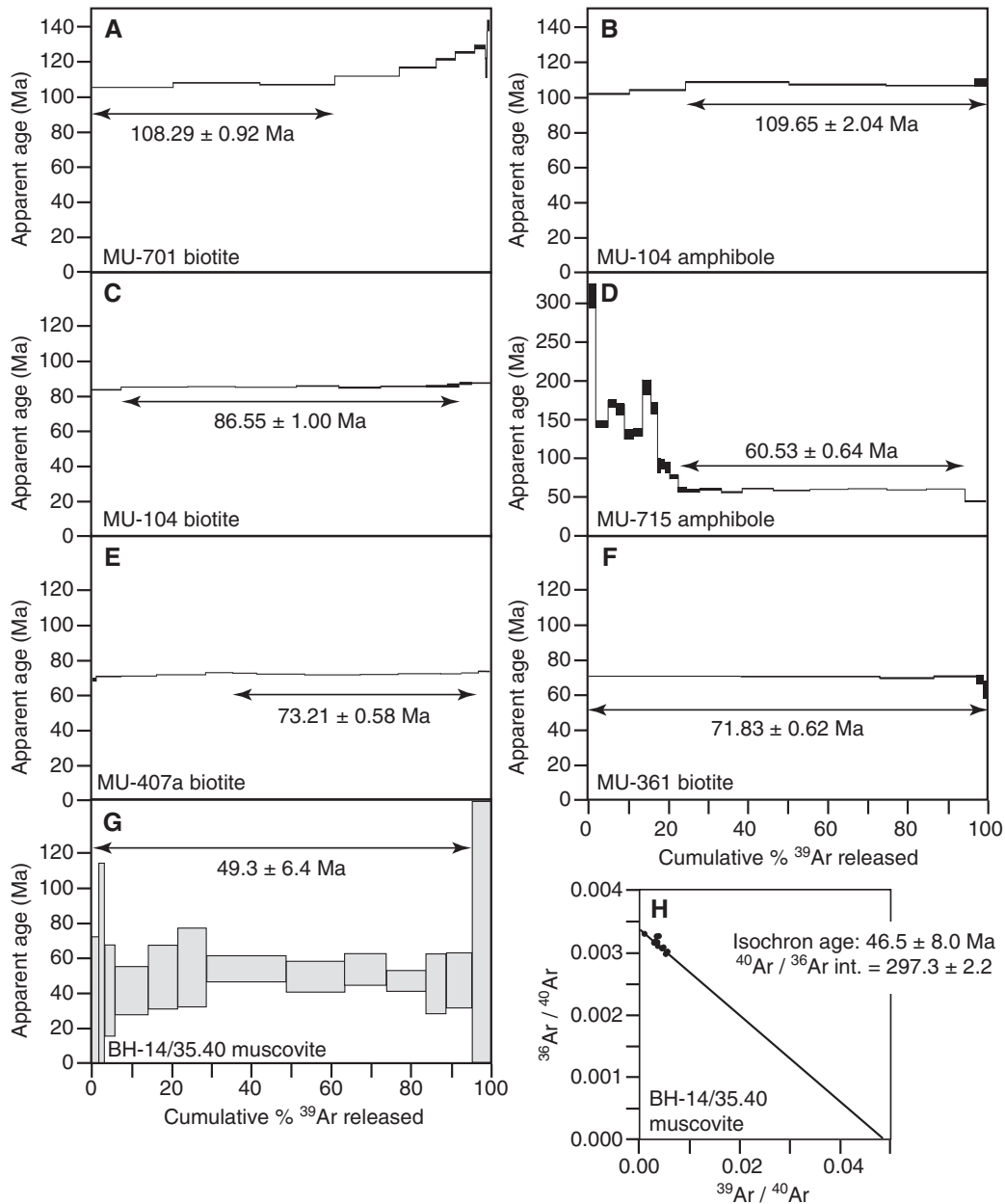


FIG. 9. A. to G. Age spectra of $^{40}Ar/^{39}Ar$ age incremental-heating results from amphibole, biotite, and muscovite samples of the Muteh gold area (see App. 1 for detailed incremental-heating data for each sample). F. Inverse isochron age for sample BH-14/35.40 from the gold mineralization at Muteh corresponding to the age spectrum displayed in (G). Ages are calculated relative to the Taylor Creek rhyolite (28.34 Ma, Renne et al., 1998) and reported with $2\sigma$ uncertainties.

TABLE 1. Summary of $^{40}$Ar/$^{39}$Ar Age Determinations from Laser-Ablation and Incremental-Heating Experiments from the Muteh Gold Deposit Area (see Apps. 1 and 2 for details)

| Sample no. | Mineral | Location | Description | Number of ablations | Laser ablation experiments Range of ablation ages (Ma) | Weighted mean age (Ma) | Incremental heating Apparent age (Ma) |
|---|---|---|---|---|---|---|---|
| MU-701 | Biotite | Haji Qara | Metamorphosed pelite | | | | 108.29 ± 0.92 |
| MU-702 | Biotite | Haji Qara | Metamorphosed pelite | 6 | 63.7 ± 3.8 – 86.7 ± 10.2 | | |
| MU-104 | Amphibole | Chah Bagh | Amphibolite | | | | 109.65 ± 2.04 |
| MU-104 | Biotite | Chah Bagh | Amphibolite | | | | 86.55 ± 1.00 |
| MU-608 | Biotite | Ghorom Ghorom | Leucogranite | 2 | 53.63 ± 11.46 & 57.84 ± 9.32 | | |
| MU-407a | Biotite | Darreh Ashki | Mesocratic granite | | | | 73.21 ± 0.58 |
| MU-407b | Biotite | Darreh Ashki | Mesocratic granite | 5 | 56.17 ± 20.02 – 75.24 ± 14.74 | | |
| MU-361 | Biotite | East of Chah Khaton | Subhorizontal mylonite | | | | 71.83 ± 0.62 |
| MU-715 | Amphibole | North of Esfajird | Quartz-amphibole pegmatite | | | | 60.53 ± 0.74 |
| MU-717 | Amphibole | North of Esfajird | Diorite intrusion | 6 of 6 | 53.74 ± 2.30 – 55.66 ± 2.08 | 54.64 ± 1.66 | |
| MU-717 | Biotite | North of Esfajird | Diorite intrusion | 6 of 6 | 52.82 ± 4.48 – 57.03 ± 3.26 | 54.85 ± 1.00 | |
| MU-322 | Muscovite | Chah Khaton open pit | Quartz-muscovite alteration in ore zone | 5 of 5 | 41.53 ± 11.68 – 51.75 ± 11.60 | 46.19 ± 4.60 | |
| BH-14/35.40 | Muscovite | Chah Khaton borehole | Quartz-carbonate-pyrite vein in ore zone | | | | 49.3 ± 6.4 |

Notes: Ages calculated relative to the Taylor Creek rhyolite (28.34 Ma, Renne et al., 1998) ±2σ errors; weighted mean ages have only been calculated for three out of the six samples analyzed by laser ablation experiments, which are the samples that gave consistent ages during the different laser ablation experiments

lite layer (MU-104, Fig. 2) concordant to the subhorizontal foliation of the host gneiss display relatively flat, undisturbed age spectra, with an age of 109.65 ± 2.04 Ma for 75.3 percent of the total $^{39}$Ar released from amphibole (Fig. 9B), and an age of 86.55 ± 1.00 Ma for 84.4 percent of the total $^{39}$Ar released from biotite (Fig. 9C).

*Magmatic intrusions:* In situ laser ablation of biotite and amphibole from the westernmost dioritic intrusion emplaced in the metamorphic complex (MU-717, Fig. 2) yielded similar ages within error of 54.85 ± 1.00 and 54.64 ± 1.66 Ma, respectively (Table 1), based on six ablation experiments for each mineral. Incremental heating of an amphibole separate from a quartz-amphibole pegmatite crosscutting the diorite (MU-715, Fig. 2) yielded a strongly disturbed age spectrum with high and erratic apparent ages for <20 perent of $^{39}$Ar released. A plateau segment for most of $^{39}$Ar released at higher temperatures yielded an age of 60.35 ± 0.64 Ma (71.8% of $^{39}$Ar released; Fig. 9D). The K/Ca data of sample MU-715 (App. 1) shows that it is a polyphase sample, with the initial 20 to 25 percent of gas released from a very low K content mineral. Incremental heating of biotite from the leucogranite of the eastern metamorphic complex (MU-407a, Fig. 2) produced a stepwise increase of apparent ages for the early degassing increments and a plateau segment for the total $^{39}$Ar released above 30 percent. The age indicated by the plateau is 73.21 ± 0.58 Ma for 61.6 percent of the total $^{39}$Ar released (Fig. 9E). In situ laser-ablation analyses of single biotite grains from the leucogranite (MU-407b and MU-608, Fig. 2) yielded ages between 56.17 ± 20.02 and 75.24 ± 14.74 Ma (Table 1, App. 2).

*Mylonite from the eastern metamorphic complex:* A biotite separate from a gneiss with a subhorizontal mylonitic texture from the eastern metamorphic complex, but remote from any mineralized area (MU-361, Fig. 2), yielded a concordant age

spectrum with a plateau age of 71.83 ± 0.62 Ma (Fig. 9F). Although muscovite was identified in this sample, it does not occur in adequate quantities for separation. Therefore, it was not possible to date this mineral by $^{40}$Ar/$^{39}$Ar.

*Hydrothermal muscovite associated with gold mineralization, Chah Khaton (Fig. 2):* Incremental heating of muscovite from the alteration zone immediately bordering a steeply dipping quartz-pyrite vein (BH-14 35.40, Figs. 2, 6B) yielded a plateau age of 49.3 ± 6.4 Ma for 98.4 percent of total $^{39}$Ar released and an inverse isochron age of 46.5 ± 8.0 Ma (Fig. 9G-H). Five in situ laser-ablation analyses of muscovite in a quartz-carbonate-pyrite vein (Fig. 6C) from the gold orebodies (MU-322, Fig. 2) yielded a weighted mean age of 46.19 ± 4.60 Ma (Table 1, App. 2).

*Discussion of the $^{40}$Ar/$^{39}$Ar data*

The $^{40}$Ar/$^{39}$Ar age determinations reveal a coherent sequence of cooling and hydrothermal events in the metamorphic complex in the Golpaygan-Muteh area. The muscovite samples from the alteration zone and one quartz vein from the orebodies have $^{40}$Ar/$^{39}$Ar ages between 55.7 and 38.5 Ma, including analytical uncertainties, indicating that gold mineralization at Muteh postdates all other dated events (Fig. 10). This lower to middle Eocene age is consistent with the structural setting of the gold orebodies, which were emplaced along northwest-oriented normal faults that can be correlated with the Tertiary extensional tectonic event reported by Tillman et al. (1981; Fig. 10).

The overlapping $^{40}$Ar/$^{39}$Ar ages of biotite and amphibole at 54.85 ± 1.00 and 54.64 ± 1.66 Ma, respectively, from the granodiorite intrusion in the westernmost metamorphic complex (MU-717, Fig. 2) indicate rapid cooling of this intrusion and represent a lower estimate of the intrusion age of the granodiorite. It is coeval with early Tertiary gabbroic, dioritic, and
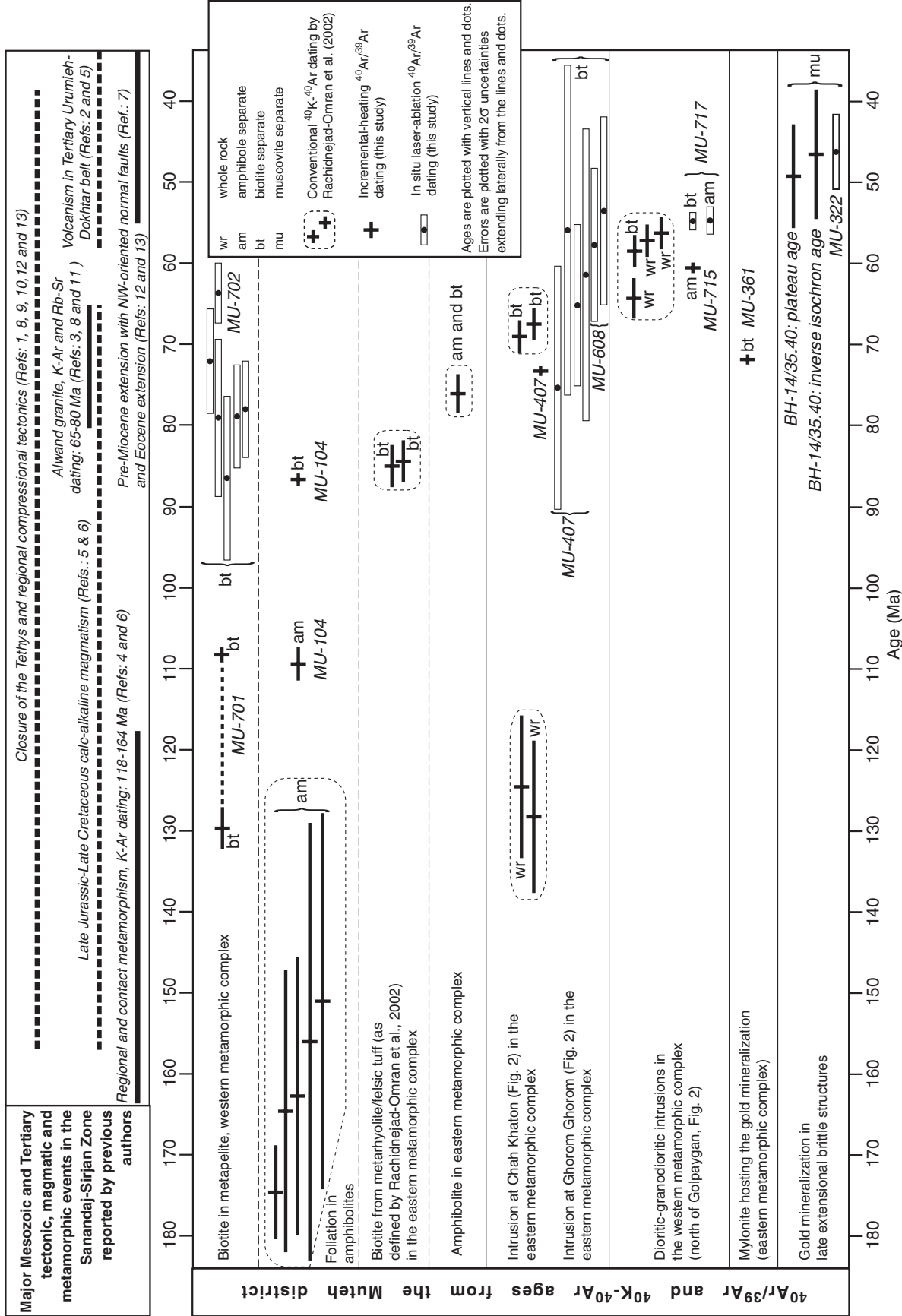
FIG. 10. Summary of $^{40}$Ar/$^{39}$Ar incremental-heating and in situ laser-ablation data (this study), and $^{40}$K–$^{40}$Ar mineral separate and whole-rock data by Rachidnejad-Omran et al. (2002) for the Muteh gold mine district, together with a summary of major tectonic, magmatic, and metamorphic events in the Sanandaj-Sirjan zone reported by previous authors. References: 1 = Stöcklin (1968), 2 = Förster (1974), 3 = Valizadeh and Cantagrel (1975), 4 = Adib (1978), 5 = Berberian and Berberian (1981), 6 = Berberian and King (1981), 7 = Tillman et al. (1981), 8 = Braud (1987), 9 = Hooper et al. (1994), 10 = Mohajjel et al. (2003), 11 = Baharifar et al. (2004), 12 = Agard et al. (2005), 13 = Ghasemi and Talbot (2006). All analytical errors are plotted with 2σ uncertainties, including those for the $^{40}$K–$^{40}$Ar data taken from Rachidnejad-Omran et al. (2002). The later authors do not explicitly indicate whether uncertainties are 1 or 2σ in their contribution, but they state that the analytical errors are quoted following Mahood and Drake (1982), who quote 1σ errors. Therefore, uncertainties indicated in table 2 of Rachidnejad-Omran et al. (2002) have been multiplied by two.

granodioritic intrusions reported elsewhere in the Sanandaj-Sirjan zone (Thiele et al., 1968; Leterrier, 1985; Braud, 1987), as well as Tertiary magmatic activity in the adjacent Urumieh-Dokhtar magmatic belt (Figs. 1, 10). Within analytical uncertainty, the $^{40}Ar/^{39}Ar$ age of the granodiorite overlaps with the whole-rock $^{40}K$-$^{40}Ar$ ages of 56 to 57 Ma reported by Rachidnejad-Omran et al. (2002) for the same intrusion (Fig. 10). The presence of a low K content phase, such as chlorite, responsible for the older apparent plateau age of 60.35 ± 0.64 Ma of the crosscutting quartz-amphibolite pegmatite (sample MU-715) must be treated with caution and should not be interpreted as a cooling age. The presence of phases such as chlorite is known to produce $^{39}Ar$ recoil, resulting in abnormal, old apparent $^{40}Ar/^{39}Ar$ ages (e.g., Lo and Onstott, 1989). Likewise, the older whole-rock and biotite $^{40}K$-$^{40}Ar$ ages between 64 and 58 Ma (Fig. 10) of Rachidnejad-Omran et al. (2002) may also be an analytical artifact due to $^{39}Ar$ recoil. Thus, the most reliable age of the granodiorite is about 54 to 55 Ma.

The $^{40}Ar/^{39}Ar$ age data indicate that gold ore formation at Muteh was contemporaneous with magmatism in the adjacent Tertiary Urumieh-Dokhtar magmatic belt (Figs. 1, 10). Moreover, within uncertainty, the age of the Eocene granodiorite intrusion emplaced in the westernmost metamorphic complex (MU-717, Figs. 2, 10) overlaps with the age of muscovite from the gold deposit (BH-14/35.40, Figs. 2, 10). Therefore, both events can be considered as coeval.

The plateau segment of biotite from the leucogranite sample MU-407a reveals that this intrusion from the eastern metamorphic complex had cooled down to about 350°C by 73.21 ± 0.58 Ma (Fig. 9E). The decreasing apparent ages of low-temperature degassing increments (Fig. 9E) suggest that biotite from the leucogranite subsequently experienced argon loss. The youngest in situ laser-ablation age of the leucogranite samples MU-407b and MU-608 suggests that the later event is younger than 53.63 ± 11.46 Ma (Table 1, App. 2). Based on the available age determinations, argon loss may be attributed to the emplacement of the early Eocene granodioritic intrusions at about 54 to 55 Ma or hydrothermal fluid circulation associated with early to middle Eocene gold mineralization between 55.7 and 38.5 Ma. The conventional $^{40}K$-$^{40}Ar$ ages of biotite separates between about 67 and 69 Ma (Fig. 10) reported by Rachidnejad-Omran et al. (2002) may only represent mixing ages of biotite cooling ages and younger overprinting magmatic or hydrothermal events.

The relatively flat and undisturbed age spectra of biotite at 71.83 ± 0.62 Ma from the mylonite zone (Fig. 9F) could be straightforwardly interpreted as the age of ductile deformation in the eastern metamorphic complex. However, flat $^{40}Ar/^{39}Ar$ age spectra from biotite have to be interpreted with great caution, because this mineral is particularly sensitive to breakdown during experimental step heating, whereby the gas does not evolve by simple volume diffusion, resulting in a loss of the spatial $^{40}Ar/^{39}Ar$ gradient by homogenization and false plateau spectra (Hanes, 1991). Apparently undisturbed but abnormally old $^{40}Ar/^{39}Ar$ age spectra can also be produced by biotite due to incorporation of excess $^{40}Ar$ introduced by an extraneous crustal fluid (e.g., Roddick et al., 1980; Renne, 1995). Given the large uncertainties of the $^{40}Ar/^{36}Ar$ intercept of the isochron calculated for this biotite sample (MU-361,

App. 1), a small amount of excess $^{40}Ar$ is possible but of uncertain significance. Finally, if a mica from a mylonite does not completely recrystallize at or below its closure temperature, it may yield abnormally "old $^{40}Ar/^{39}Ar$ ages" due to a significant gas component inherited from relict grains, and thus it only provides a maximum age for the time of deformation (West and Lux, 1993). At Muteh, such inheritance could be due to relict biotite grains from the leucogranite, which has a cooling age of 73.21 ± 0.58 Ma (Fig. 9E), just slightly older than the age of the biotite from the mylonite (Fig. 9F). Therefore, the flat age spectra of 71.83 ± 0.62 Ma of the biotite should only be considered as a maximum age estimate of ductile deformation in the eastern metamorphic complex, whereas the 55.7 to 38.5 Ma muscovite ages from the gold deposit define a lower age limit for the ductile deformation event.

The flat and relatively undisturbed 109.65 ± 2.04 and 86.55 ± 1.00 Ma plateau ages of amphibole and biotite, respectively, from the amphibolite layer in the eastern metamorphic complex (MU-104, Fig. 9B-C) reflect cooling of the latter below the closure temperatures of the respective minerals (550° ± 50° and 350° ± 50°C for amphibole and biotite, respectively, see McDougall and Harrison, 1999) and could be related to metamorphism of the rocks from the eastern complex. The conventional $^{40}K$-$^{40}Ar$ biotite ages of 85 Ma by Rachidnejad-Omran et al. (2002) for a metarhyolite and/or tuff in the eastern part of the metamorphic complex (Fig. 10) is likely also related to the same cooling event during retrograde metamorphism, whereas the geologic significance of the conventional $^{40}K$-$^{40}Ar$ mixed amphibole-biotite age of about 76 Ma by Rachidnejad-Omran et al. (2002) for mafic rocks from the same part of the metamorphic complex (Fig. 10) should be viewed with caution, as it may represent mixing ages because of recent argon loss. The $^{40}Ar/^{39}Ar$ plateau segment at 108.29 ± 0.92 Ma followed by a rising staircase pattern to higher apparent ages in biotite from sample MU-701 of the western metamorphic complex (Fig. 9A) together with the lower ablation ages of sample MU-702 between 63.7 ± 3.8 and 86.7 ± 10.2 Ma (Table 1, App. 2) reveal some heterogeneity in these biotites that are difficult to interpret. Biotites from metamorphosed pelite in the western metamorphic complex are disturbed samples from which a single cooling age cannot be inferred from the available data.

## Fluid Inclusion Microthermometry and Raman Spectroscopy

### Methodology

Microthermometric measurements were made on 100-$\mu$m-thick doubly polished wafers with a Fluid Inc. adapted USGS gas-flow heating-freezing stage (Werre et al., 1979; Woods et al., 1981) mounted on a Leitz Laborlux S microscope equipped with a Nikon 40× ELWD long focus lens and on a Linkam THMGS-600 stage mounted on a DMLB Leica microscope equipped with a Nikon 100×long working distance lens. The systems were calibrated with synthetic fluid inclusions (Sterner and Bodnar, 1984) at temperatures of –56.6°, 0.0°, and 374.1°C. Precision and accuracy were ±0.1°C between –70° and 40°C, ±2°C below –70°C, and ±1°C above 100°C. Gases were identified with a Labram

Raman spectrometer using a Nd-YAG laser (532-nm wavelength). Clathrate melting was used to calculate the salinity of $CO_2$-bearing fluid inclusions with the equation of Chen (1972, cited in Diamond, 1992) for inclusions in which clathrate melting occurred before homogenization of the $CO_2$ liquid and gaseous phases, whereas the procedure described in Diamond (1992) was used for inclusions showing homogenization of the $CO_2$ liquid and gas phases before breakdown of clathrate on heating. The salinity of aqueous fluid inclusions devoid of dissolved gases was calculated with the equation of Bodnar (2003).

*Fluid inclusion petrography*

The fluid inclusion study was undertaken on barren, regional quartz veins concordant with the foliation of the host metapelite, on quartz from metapelite, and on quartz veins and quartz from silicified host rocks from gold orebodies of the Chah Khaton open pit (loc. 1, Fig. 2). Four fluid inclusion types were recognized in this study on the basis of the number of phases at room temperature and their microthermometric behavior.

Type I inclusions are liquid rich and contain two phases at room temperature (Fig. 11A-B). In the majority of the inclusions, the vapor bubble typically occupies about 10 percent of the total inclusion volume. Some of the inclusions have a regular, subrounded square to rectangular shape, whereas others are more irregular and show characteristic reequilibration textures, such as annular or decrepitated inclusions surrounded by a cluster of smaller inclusions (Fig. 11A). The size of the inclusions varies between 2 and 10 $\mu$m. Type II inclusions are vapor-rich (Fig. 11B). Optically the vapor phase occupies the entire volume of the inclusion, although in reality approximately up to 10 volume percent liquid surrounding the vapor phase may go unnoticed in such inclusions. Type II inclusions have a regular subrounded, square to rectangular shape, and a size of 2 to 10 $\mu$m. Type I and II inclusions only occur in regional quartz veins and quartz from metapelite. They have never been observed in the late-stage gold-bearing quartz veins. They occur predominantly in clusters or along trails, which crosscut grain boundaries of quartz, subsidiary isolated inclusions of both types have also been observed. Therefore, they are interpreted as secondary fluid inclusions. Type I and II fluid inclusions are contemporaneous, since they can be found in the same trail (Fig. 11B).

Type III inclusions are liquid rich and contain two phases at room temperature with the bubble occupying 5 to 15 percent of the total inclusion volume. The inclusions are small and subrounded, with sizes generally less than 5 $\mu$m (Fig. 11C). Type III inclusions are only present in late-stage quartz-carbonate-pyrite veins, most commonly in euhedral quartz (Fig. 6C), the silicified host rocks at the gold occurrences, and in regional quartz veins in the immediate vicinity of the orebodies. They occur either in small clusters or are isolated. There are no textural features in euhedral quartz from the gold-bearing quartz veins that allowed us to define a primary nature for these inclusions (e.g., growth zones). Therefore, type III inclusions must be regarded as secondary, although a primary nature cannot be ruled out.

Type IV inclusions are liquid rich, with one to two phases at room temperature. The two-phase inclusions contain a small
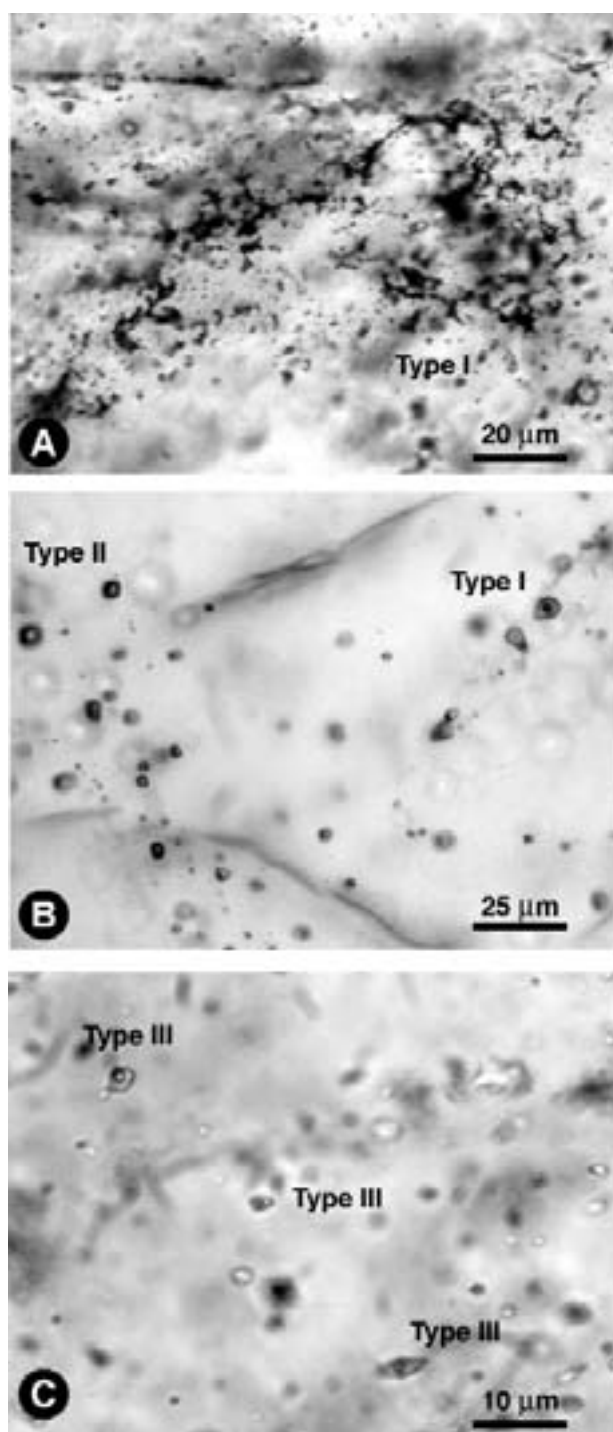


FIG. 11. Fluid inclusions observed in the district of the Muteh gold mine. The host mineral in all plates is quartz. A. Reequilibration textures of regional type I fluid inclusions. B. Distinct trails of type I, liquid-dominated $H_2O$-$CO_2$-NaCl $\pm$ $N_2$ $\pm$ $CH_4$ inclusions and type II, vapor-dominated $CO_2$ $\pm$ $N_2$ $\pm$ $CH_4$ inclusions. C. Type III $H_2O$-$CO_2$-NaCl inclusions from the gold-bearing quartz-carbonate-pyrite veins and their immediate host rocks at Chah Khaton open pit (see loc. 1, Fig. 2).

vapor bubble at room temperature, filling 1 to 5 percent of the total inclusion volume. These inclusions are the largest, with sizes up to 15 $\mu$m. Type IV inclusions occur as secondary

fluid inclusions in late-stage gold-bearing veins and regional quartz veins.

## *Microthermometric fluid inclusion and Raman spetrographic data*

The microthermometric data are summarized in Figure 12. Type I fluid inclusions display four phase transitions (Fig. 12A-D): (1) $CO_2$-melting between $-58.9°$ and $-56.9°C$; (2) clathrate-melting between $-1.8°$ and $+8.9°C$, mostly between $+1.2°$ and $+5.9°C$; (3) homogenization of $CO_2$ to the liquid phase between $+8.3°$ and $+23.6°C$ (with one outlier at $-3.3°C$); and (4) total homogenization temperatures to the liquid phase between $+186.1°$ and $+294.5°C$, except two outliers at $+164.2°$ and $+304.5°C$. A limited number of inclusions decrepitated before reaching total homogenization. In addition, a few final ice-melting temperatures (in 11 inclusions) were recorded between $-17.2°$ and $-6.7°C$ (not shown in Fig. 12). Melting of clathrate systematically occurred in equilibrium with liquid $H_2O$ and both liquid and gaseous $CO_2$. The clathrate-melting temperatures correspond to a salinity range between 2.2 and 17.5 wt percent NaCl equiv, with most of them grouped between 7.6 and 14.2 wt percent NaCl equiv. Type II inclusions yielded (1) melting temperatures of $CO_2$ between $-59.1°$ and $-57.0°C$; (2) a few clathrate-melting temperatures (in six inclusions) were recorded between $+7.4°$ and $+9.4°C$; and (3) homogenization of $CO_2$ to the liquid phase occurred between $-23.8°$ and $+20.8°C$ (Fig. 12E-G). The clathrate-melting temperatures correspond to salinities between 2.8 and 7.2 wt percent NaCl equiv and indicate that a thin rim of $H_2O$ is present around the $CO_2$ phase.

The $CO_2$-melting temperatures below $-56.6°C$ in both type I and II inclusions reveal the presence of other dissolved gases. Raman spectra of the gas phase in type I and II inclusions show two peaks at 1,283 and 1,387 $cm^{-1}$, diagnostic of $CO_2$, and one peak at 2,330 $cm^{-1}$ revealing the presence of dissolved $N_2$. In addition, a small peak at 2,913 $cm^{-1}$ in the gas-rich type II inclusions is diagnostic for the presence of small amounts $CH_4$ in these fluids. Thus, the regional fluid trapped in type I and type II inclusions is a saline $H_2O$-$CO_2$-NaCl fluid with minor concentrations of $N_2$ (less than 8 mole %) and traces of $CH_4$.

The majority of type III inclusions only showed two-phase changes during the microthermometric study. Clathrate melting was measured between $+3.0°$ and $+8.7°C$, with a majority of measurements falling between $+7.0°$ and $+8.7°C$ (Fig. 12H), and total homogenization temperatures to the liquid phase fall between $+155.7°$ and $+301.8°C$, with a peak between $+210°$ and $+230°C$ (Fig. 12J). A few inclusions ($n$ = 9) show ice melting, mainly between $-3.0°$ and $-4.6°C$, with one outlier at $-9.3°C$ (Fig. 12I). Inclusions from the same fluid inclusion assemblage have fairly homogeneous clathrate-melting temperatures, whereas total homogenization temperatures can vary by several tens of degrees. The clathrate melting indicates the presence of dissolved gases, identified as $CO_2$ by Raman spectroscopy with diagnostic peaks at 1,285 and 1,388 $cm^{-1}$. No other dissolved gas was detected by Raman spectroscopy. Neither liquid $CO_2$ nor any melting behavior at or below the triple point of $CO_2$ ($-56.6°C$) was visible in type III inclusions, despite repeated careful checks of larger inclusions. It is concluded that type III inclusions only

contain a small mole percentage of low-density $CO_2$ (below the critical density of $CO_2$: 0.468 $g/cm^3$) and that clathrate dissociates on heating in the presence of aqueous liquid and $CO_2$ vapor but the absence of liquid $CO_2$. For the phase transition: clathrate + gaseous $CO_2$ + $H_2O$ (liquid) → gaseous $CO_2$ + liquid $H_2O$, the melting temperature of clathrate between $-1.48°$ and $+10°C$ is a function of both fluid salinity and $P_{CO_2}$ (Collins, 1979; Hedenquist and Henley, 1985). Therefore, using the equation of Chen (1972) for the clathrate data gathered from type III fluid inclusions overestimates their salinity. Thus, the salinities between 2.6 and 11.9 wt percent NaCl equiv deduced from the clathrate-melting temperatures of type III inclusions, with a peak at about 4 wt percent NaCl, must only be considered as upper salinity estimates. Nevertheless, the tight clustering of most clathrate-melting temperatures between $+7.0°$ and $+8.7°C$ (Fig. 12H) suggests a fairly constant salt content and $P_{CO_2}$ in type III inclusions. In conclusion, type III inclusions are interpreted as a low-salinity aqueous fluid with a dilute, low-density $CO_2$ component.

In the two-phase type IV inclusions, final ice-melting temperatures range between $-26.9°$ and $-20.7°C$ with a data peak between $-23°$ and $-24°C$ (Fig. 12K). Ice typically starts to melt at temperatures below $-42°C$, thus indicating the presence of additional cations besides $Na^+$, interpreted as $Ca^{2+}$. Total homogenization temperatures fall between $+55.4°$ and $+190.6°C$ with a majority of values between $+100°$ and $+150°C$ (Fig. 12L).

## *Discussion of the fluid inclusion data*

Type I and II fluid inclusions trapped in metamorphic quartz segregation veins and in quartz metapelite are the oldest fluid inclusion types recognized in this study. Their coexistence in some fluid inclusion trails and clusters reveals local unmixing of a moderately saline $H_2O$-$CO_2$ fluid in the metamorphic rocks. Such fluids and unmixing processes are common in greenschist to granulite facies metamorphic rocks (e.g., Sisson et al., 1981; Touret, 1981; Yardley and Bottrell, 1988). The vast majority of fluid inclusions in such quartz veins, which may have recrystallized during the metamorphic cycle and undergone extensive fracturing, contain secondary fluid inclusions that have been trapped during their return to the surface. The annular inclusions and the decrepitated inclusions surrounded by a cluster of smaller inclusions (Fig. 11A) are evidence for reequilibration after their entrapment during the retrograde evolution of the metamorphic complex (Boullier et al., 1991; Vityk and Bodnar, 1995). The elevated salinities of the regional type I fluid inclusion types, including those from the western metamorphic complex with salinities up to 17.5 wt percent NaCl equiv, are not uncommon in greenschist to granulite facies metamorphic rocks (Yardley and Graham, 2002). In the case of the metamorphic complex at Muteh, several different sources or processes could account for the high fluid salinities. These include metamorphism of evaporite-bearing sedimentary rock units (e.g., Rich, 1979; Mora and Valley, 1989; Oliver et al., 1992; Giuliani et al., 1995). Indeed, the presence of subordinate scapolite in marble interlayered with metapelite in the western metamorphic complex of the Muteh area is likely evidence of metaevaporites (Kwak, 1977; Moine et al., 1981; Faryad, 2002). A further possible
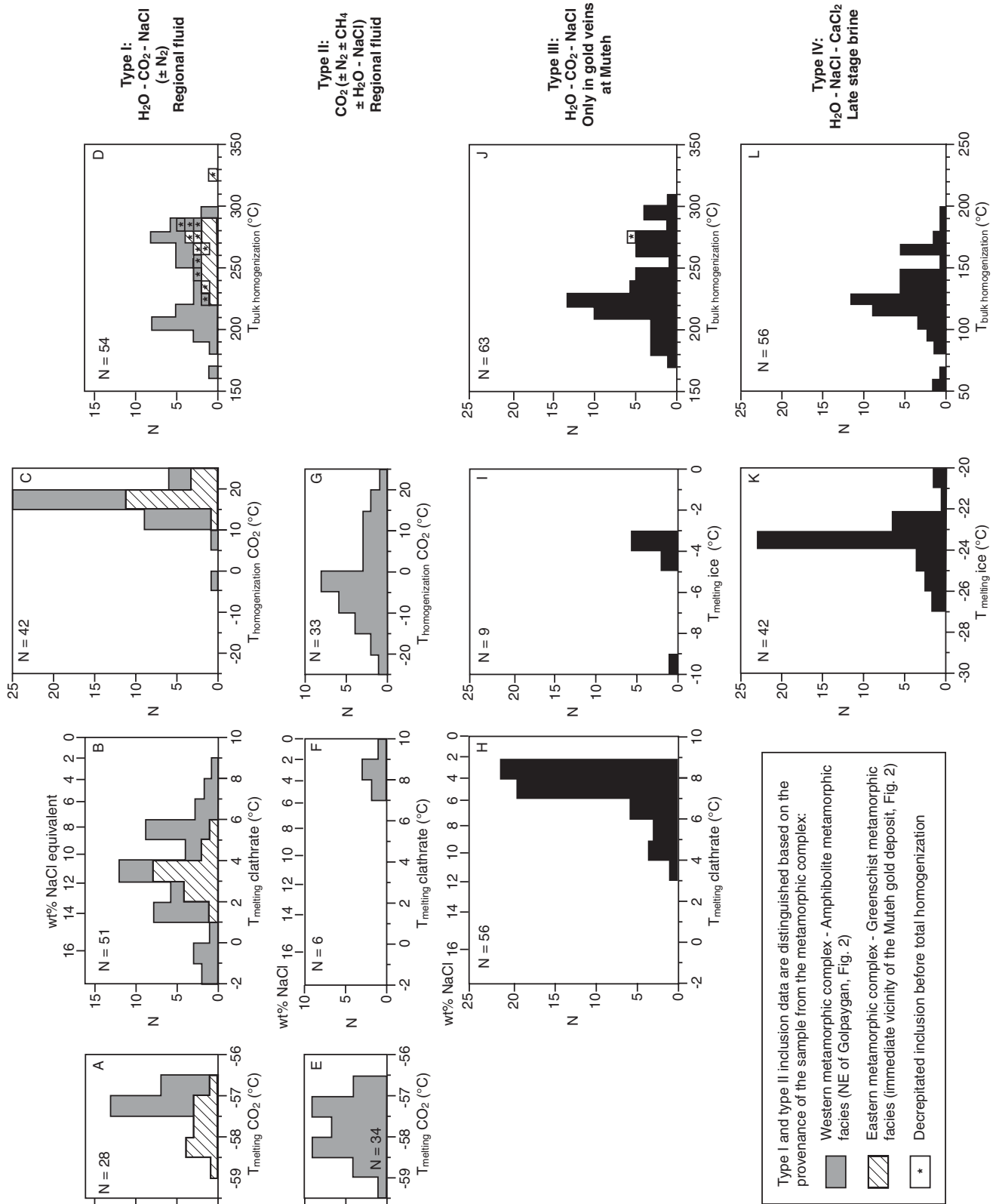
Fig. 12. Fluid inclusion microthermometric data from regional metamorphic quartz veins and late-stage quartz–carbonate–pyrite veins from the gold orebodies at the Chah Khaton open pit (see loc. 1, Fig. 2).

source of saline fluids coexisting with $CO_2$-rich fluids are magmatic intrusions (e.g., Nabelek and Ternes, 1997; Baker, 2002) emplaced at various stages during the evolution of the Sanandaj-Sirjan zone. Alternatively, metamorphic processes such as retrograde hydration reactions in fluid-starved crystalline rocks (Bennett and Barker 1992; Yardley and Valley 1997) or amphibolite facies metamorphism of impure marbles and migmatization (as reported by Rachidnejad-Omran et al., 2002) could explain the coexistence of a highly saline fluid with a $CO_2$-rich fluid (e.g., Sisson et al., 1981; Touret, 1985; Trommsdorf et al., 1985 ; Shmulovich et al., 1994) in metamorphic rocks and quartz segregation veins at Muteh.

Type III fluid inclusions are only encountered in quartz-carbonate-pyrite veins from the gold orebodies and their immediate host rocks. Therefore, it is concluded that they postdate regional metamorphism and ductile deformation of the host rocks and that they are most likely related to the Eocene gold ore-forming process. The large range of homogenization temperatures between about 170° and 310°C of type III inclusions (Fig. 12J) and the variable homogenization temperatures within the same fluid inclusion assemblage reveal that type III inclusions have reequilibrated to different pressure-temperature conditions during postore evolution of the metamorphic complex. However, the majority of the clathrate-melting temperatures fall between +7.0° and +8.7°C (Fig. 12H), suggesting relatively constant fluid compositions, with maximum salinities between 2.6 and 5.8 wt percent NaCl equiv. We conclude that the compositional information of the fluid trapped during ore formation has been preserved. The relatively low salinity and low $CO_2$-concentration of the type III fluid trapped within the late-stage quartz-carbonate-pyrite veins contrasts with the distinctly higher salinity and $CO_2$ contents of the type I regional fluids. Two interpretations can be offered: (1) either formation of the gold ore deposits at Muteh was linked to the introduction of a distinct low-salinity, low $CO_2$ content aqueous fluid during Eocene crustal extension, unrelated to and postdating the highly saline and $CO_2$-rich regional metamorphic-magmatic type I and II fluids, or (2) type III fluid in the gold deposits could possibly result from mixing of the regional type I fluid with a dilute, aqueous fluid, such as meteoric water. The distinctly later timing and fairly constant composition of type III fluids, as revealed by the relatively narrow range of clathrate-melting temperatures (Fig. 12H), argues against the second interpretation. Such low-salinity, low $CO_2$ content aqueous fluids are typical for both orogenic and intrusion-related gold deposits (Ridley and Diamond, 2000; Baker, 2002).

Type IV inclusions are late, low-temperature brines that have circulated in the metamorphic complex after or during the latest stages of gold ore formation at Muteh.

### Origin of the Gold Deposits at Muteh: Orogenic or Intrusion Related?

The $^{40}Ar/^{39}Ar$ dating indicates that gold ore formation at Muteh was early to middle Eocene in age and significantly younger than the Precambrian to Paleozoic ages advocated in earlier studies by Thiele et al. (1968), Samani (1988), Paidar-Saravi (1989), and Rachidnejad-Omran et al. (2002). This conclusion is also supported by the important role of brittle extension on the geometry of the ore veins and the late-stage

hydrothermal alteration postdating the ductile fabric and the metamorphic assemblage of the host rocks, respectively. The 55.7 to 38.5 Ma $^{40}Ar/^{39}Ar$ age reveals that gold mineralization at Muteh is unrelated to the leucogranite-granite-granodiorite intrusions that crop out in the eastern metamorphic complex (intrusions shown in black in Fig. 2), as the latter have biotite cooling ages of about 73 Ma and are overprinted by ductile deformation, which in turn is cut by the normal northwest-oriented faults and veins controlling the gold mineralization at Muteh. This refutes the model of Thiele et al. (1968) and Samani (1988), suggesting a genetic link between the gold deposit and leucogranite in the eastern metamorphic complex. The age relationships are also at odds with the Paleozoic exhalative hot-spring model of Rachidnejad-Omran et al. (2002). A direct link between metamorphism of the host rocks and ore formation as suggested by Paidar-Saravi (1989) is also questioned by our $^{40}Ar/^{39}Ar$ data. The $^{40}Ar/^{39}Ar$ cooling ages of biotite and hornblende at about 86 and 109 Ma, respectively, from the concordant amphibolite layer in the metamorphic complex indicate that regional retrograde metamorphism preceded gold mineralization by several tens of millions of years. It is unlikely that retrograde metamorphism could have sustained continuous, regional fluid circulation for 40 m.y. or more.

Our study shows that gold ore formation at Muteh was contemporaneous with a period of Tertiary crustal extension reported by Tillman et al. (1981) and with magmatism in the immediately neighboring Tertiary Urumieh-Dokhtar belt (Fig. 1). Within analytical uncertainty, the Eocene granodiorite intrusion emplaced in the westernmost metamorphic complex (MU-717, Fig. 2) is coeval with the formation of the gold deposit at Muteh (Fig. 10). Although a genetic link between gold mineralization and Tertiary magmatism is permissible based on radioisotopic age relationships on a regional scale, the dated Eocene granodiorite, located approximately 40 km to the west of Muteh (Fig. 2) appears too distant to be directly linked to the gold mineralization event. A coeval, local intrusion remains to be documented. Alternatively, metamorphic processes cannot be entirely ruled out, because the gangue and alteration mineralogy, including quartz, sericite, albite, carbonate, and chlorite, and the dilute, $CO_2$-bearing aqueous fluid inclusions from the gold orebodies are characteristic of both orogenic and intrusion-related gold deposits (Cassidy and Bennett, 1993; Mikucki and Ridley, 1993; Ridley and Diamond, 2000; Lang and Baker, 2001; Baker, 2002). Tillman et al. (1981) linked pre-Miocene extensional tectonics to continuous underthrusting along the boundaries of the Sanandaj-Sirjan zone. Therefore, dehydration of such underthrusted rocks might have been a source of ore-forming fluids, which could have escaped along the extensional structures hosting the orebodies at Muteh. However, the extensional structural setting during exhumation of the metamorphic host-rock complex and gold ore formation at Muteh is a clearly distinct feature, which significantly differs from the majority of orogenic gold deposits, where orebodies are typically hosted by reverse component shear zones, which were formed during a main phase of crustal shortening in compressional or transpressional regimes (Groves et al., 2003; Goldfarb et al., 2005). Thus, with the present state of knowledge, principally based on the radioisotopic age relationships and the extensional

structural setting, an intrusion-related model is considered as more plausible than an orogenic model for the Muteh gold deposit.

### Link between Eocene Gold Ore Formation and Exhumation of the Metamorphic Host Rocks

Since the gold orebodies at Muteh are controlled by late, brittle extensional structures that cut metamorphic rocks in the Sanandaj-Sirjan zone, it is necessary to address the link between Eocene gold ore formation and the geologic evolution of the metamorphic rocks, in particular exhumation of the metamorphic complex. As summarized by Ring et al. (1999), exhumation of metamorphic rocks occurs as a result of ductile thinning, erosion, and normal faulting. The subhorizontal foliation in the metamorphic complex at Muteh (Figs. 3A, 4A-B) confirms that ductile thinning was involved in the exhumation of the metamorphic complex (Ring et al., 1999). Ductile thinning of the host rocks occurred prior to the emplacement of the Eocene gold orebodies along normal faults (Fig. 4E-F), since the brittle structures cut the subhorizontal ductile fabric of the host rocks (Fig. 4A).

Exhumation of metamorphic domes in several orogens is accompanied by the formation of sedimentary basins (e.g., Echtler and Malavieille, 1990; Chauvet and Dallmeyer, 1992; Cassard et al., 1993; Neubauer et al., 1995; Bonev et al., 2006). At Muteh, coarse clastic Eocene sedimentary rocks, including conglomerate alternating with sandstone, sandy shale, and volcanic rocks, overlie older rock formations with a distinct unconformity (Thiele et al., 1968; Fig. 2) and are defined as syntectonic conglomerates by Alavi (1994). According to Tillman et al. (1981), the Tertiary sedimentary depocenters in the study area were structurally controlled by northwest-oriented block-bounding faults, and their consistent occurrence along the southern side of major faults supports a syntectonic origin. Further detailed studies are required to precisely document the relative timing between Eocene erosion, sedimentation, and gold ore formation at 55.7 to 38.5 Ma, and to investigate whether the Eocene sedimentary rocks formed in supradetachment basins as a consequence of metamorphic complex exhumation (e.g., Friedmann and Burbank, 1995).

Normal faulting within the metamorphic complex at Muteh is expressed by high-angle faults, which host the Eocene gold orebodies (Fig. 4E-F). The northeast-southwest extension during brittle deformation of the metamorphic basement rocks, manifested by the northwest-oriented normal faults controlling the gold ore mineralization (Figs. 3B, 4A, 6 E-F), is parallel to the extension that occurred during earlier ductile thinning, as shown by the subhorizontal northeast-oriented stretching lineation within the flat-lying foliation of the metamorphic complex (Fig. 3A). Thus, both ductile and brittle structures can be interpreted within a single, continuous extensional and exhumation event, which started with ductile deformation and gradually changed into low-grade, brittle deformation. Similar continuous ductile to brittle evolution during exhumation of metamorphic complexes has been documented in other extensional tectonic settings (e.g., Miller et al., 1983; Lee et al., 1987; Davis, 1988; Lister and Davis, 1989; Chauvet and Dallmeyer, 1992). In addition to high-angle faults, low-angle detachment surfaces participate in the

exhumation of metamorphic rock complexes in many orogens (Wernicke and Burchfield, 1982; Hodges et al., 1987; Selverstone, 1988; Lister and Davis, 1989; Teyssier and Whitney, 2002; Bonev et al., 2006). The subhorizontal breccia horizon (Figs. 2, 3E-F) located between the greenschist facies metamorphic rocks with a mylonitic fabric and the overlying unmetamorphosed and nonpenetratively deformed sedimentary rocks is interpreted as the location of such a detachment surface at Muteh. The clasts of metamorphic rocks with a mylonitic fabric within the breccia horizon (Fig. 4F) are interpreted as the result of upward transport of once deep-seated metamorphic rocks along the detachment surface and across the ductile-brittle transition (e.g., Lister and Davis, 1989). In the vicinity of the Muteh gold deposit, kinematic indicators observed in mylonitic metamorphic rocks reveal a subhorizontal shear sense with a top to the northeast displacement (Fig. 5). Such a displacement is opposite to the regional southwest-verging thrust kinematics of the Sanandaj-Sirjan tectonic zone during the Zagros orogeny and is likely the result of low-angle normal faulting during exhumation of the metamorphic complex. The extensional tectonics prior to and during Eocene gold deposition in the metamorphic basement rocks at Muteh is consistent with an overall regional, compressional tectonic setting, dominated by thrusting toward the southwest during most of the Tertiary (e.g. Alavi, 1994; Mohajjel et al., 2003; Agard et al., 2005). Indeed, contemporaneous extension and compression have been documented in a number of other orogenic belts (Neubauer et al., 1995; Hodges et al., 1996; Searle, 1999; Schoonover and Osozawa, 2004).

The northwest-oriented normal faults controlling gold ore formation at Muteh cut the subhorizontal ductile fabric of the metamorphic rocks. Therefore, we conclude that gold deposition at Muteh occurred during or after late stages of brittle extension as a result of exhumation of the metamorphic complex. According to Kouhestani (2005) and Kouhestani et al. (2005), ore formation may have started under ductile conditions at Chah Bagh (ore zone loc. 9, Fig. 2). The extensional tectonic setting provided the favorable conditions of enhanced permeability and created the favorable plumbing system for late-stage fluid circulation and ingress of a low-salinity, low $CO_2$ content aqueous fluid (type III fluid inclusions, see above) into the eastern metamorphic complex. The variable homogenization temperatures of the type III fluid inclusions (Fig. 12J), even within the same fluid inclusion assemblage, reflect reequilibration to different pressure-temperature conditions after the fluid was trapped during ore formation. Such fluid inclusion reequilibration can be interpreted as a consequence of uplift and/or ongoing exhumation (due to normal faulting and/or erosion?) of the metamorphic complex after ore formation. The formation of gold deposits at Muteh as a result of metamorphic complex exhumation is comparable to other ore deposits along the Tethyan Eurasian metallogenic belt, such as the Miocene Angouran Zn-Pb-Ag deposit in the northwestern part of the Sanandaj-Sirjan zone (Gilg et al., 2006; see loc. Ang, Fig. 1A), in the Eastern European Alps within the Tauern metamorphic core complex (Horner et al., 1997; Amann et al., 2002), in southeastern Europe (e.g., Marchev et al., 2004; Seidel et al., 2005; Marton et al., 2006; Yigit, 2006), or within the North American

cordillera (e.g., Beaudoin et al., 1991). The gold deposits at Muteh also share a comparable tectonic setting with the low-angle detachment-related deposits described in the Western United States (e.g., Spencer and Welty, 1986; Roddy et al., 1988; Ashley, 1991; Long, 1992; Losh et al., 2005). However, there are notable differences. For instance, the primary spec-ular hematite and massive K-feldspar replacement recog-nized in many low-angle detachment-related deposits in the Western United States are lacking at Muteh, and albite, which is a predominant mineral in the alteration and gangue assemblage at Muteh, is typically absent in the North Ameri-can detachment-related gold deposits. By contrast, the report by Kouhestani (2005) and Kouhestani et al. (2005) of sulfide-bearing siliceous lenses parallel to the subhorizontal mylonitic foliation in the westernmost gold occurrence at Chah Bagh (ore zone loc. 9, Fig. 2), as well as the presence of epidote in the alteration assemblage, are reminiscent of the partly sub-horizontal, tabular development of orebodies along low-angle detachment surfaces typically described in the gold deposits of the Western United States.

## Geodynamic Setting during
## Eocene Gold Ore Formation at Muteh

Slab detachment during the Eocene has been suggested by Agard et al. (2005) and Ghasemi and Talbot (2006) to explain, respectively, mafic intrusive activity at 40 to 38 Ma within the Sanandaj-Sirjan zone (Leterrier, 1985; Braud, 1987) and Ter-tiary postsuturing, calc-alkaline magmatism of the Urumieh-Dokhtar magmatic belt, located to the east of the Sanandaj-Sirjan zone (Fig. 1A). According to Davies and von Blanckenburg (1995) and De Boorder et al. (1998), the main consequences of slab breakoff within an orogen are (1) a modification of the thermal, and by extension magmatic, regime within the crust due to the emplacement of hot as-thenospheric material at shallow levels, which increases the heat flux into the continental lithosphere; (2) buoyant ascent of crustal sheets leading to rapid exhumation of high-grade metamorphic facies rocks; (3) a generalized uplift of the oro-gen due to a transient increase in the geothermal gradient; and (4) increased fluid activity in the crust and influx of fluids from the hot mantle wedge asthenosphere. It is clear that with our present-day level of knowledge, the slab breakoff scenario during Eocene geodynamic evolution of the Sanan-daj-Sirjan zone and the Urumieh-Dokhtar magmatic belt is only a working hypothesis. Nevertheless, the slab detachment model is consistent with the exhumation of metamorphic rocks, extensional tectonics, melting, intrusive activity, and an increased geothermal gradient and fluid activity at Muteh during the Eocene, creating the favorable environment for gold ore formation. If correct, then the gold mineralization event during extensional tectonics between 55.7 and 38.5 Ma at Muteh might be the direct expression of the regional ther-mal and tectonic modifications and fluid input resulting from slab breakoff beneath the Sanandaj-Sirjan zone.

## Conclusions

Gold ore formation at Muteh in Western Iran is early to middle Eocene in age and is the result of a protracted geo-logic evolution of the Sanandaj-Sirjan tectonic zone as a con-sequence of the closure of the Tethys ocean during the Zagros orogeny. Detailed field observations and precise $^{40}Ar/^{39}Ar$ dating reveal that formation of the Muteh gold deposit was related to normal faulting as a result of Eocene crustal exten-sion during the final stages of exhumation of a metamorphic rock complex. The $^{40}Ar/^{39}Ar$ data show that ore formation at Muteh was coeval with magmatism in the adjacent Tertiary Urumieh-Dokhtar magmatic belt and with nearby intrusive activity within the Sanandaj-Sirjan zone. However, a coeval magmatic event remains to be documented in the immediate neighborhood of the Muteh deposit. Based on the gangue and alteration mineralogy, and the dilute and $CO_2$-bearing aqueous fluids associated with ore formation, genesis of the Muteh gold deposit as a result of metamorphic processes (i.e., orogenic gold) cannot be excluded.

The transient increase in the geothermal gradient, as a re-sult of metamorphic rock exhumation and/or Tertiary mag-matic activity, accompanied by late, brittle extension provid-ing enhanced permeability, created the favorable plumbing system for Eocene hydrothermal fluid circulation and gold deposition. Our results and interpretations refute previous models advocating Precambrian to Paleozoic ages of mineral-ization and those linking the Muteh gold deposit to local leucogranites, exhalations associated with rhyolitic-acidic tuffs, or metamorphism of the immediate host rocks. Our study also suggests that other terranes in the Sanandaj-Sirjan zone should be considered as favorable targets for gold ex-ploration, where Tertiary extensional tectonics, coupled with deep metamorphic and/or magmatic processes could be documented.

The formation of the Muteh gold deposit as a result of ex-humation of a metamorphic rock complex, extensional tec-tonics, and possibly local magmatism during the late stages of the Zagros orogeny is comparable to the formation of other ore deposits within the Tethyan Eurasian metallogenic belt. Slab breakoff has been suggested during the Eocene geody-namic evolution of the Sanandaj-Sirjan zone and the Tertiary Urumieh-Dokhtar magmatic belt. Although still speculative, such a geodynamic setting may have provided the favorable environment for the exhumation of metamorphic rocks, ex-tensional tectonics, an increased geothermal gradient, and abundant hydrothermal fluid circulation during gold ore for-mation at Muteh.

## Acknowledgments

Tehran) and M. Hannington for reviews, comments, and editorial improvements.

*June 6, October 12, 2006*

## REFERENCES

Adib, D., 1978, Geology of the metamorphic complex at the southwestern margin of the Central-Eastern Iranian microplate (Neyriz area): Neues Jahrbuch für Geologie und Paläontologie-Abhandlungen, v. 156, p. 393–409.

Agard, P., Omrani, J., Jolivet, L., and Mouthereau, F., 2005, Convergence history across Zagros (Iran): Constraints from collisional and earlier deformation: International Journal of Earth Sciences, v. 94, p. 401–419.

Alavi, M., 1994, Tectonics of the Zagros orogenic belt of Iran: New data and interpretations: Tectonophysics, v. 229, p. 211–238.

Alavi, M., and Mahdavi, M.A., 1994, Stratigraphy and structures of the Nahavand region in western Iran and their implications for the Zagros tectonics: Geological Magazine, v. 131, p. 43–47.

Alavi, M., Vaziri, H., Seyed-Emami, K., and Lasemi, Y., 1997, The Triassic and associated rocks of the Nakhlak and Aghdarband areas in central and northeastern Iran as remnants of the southern Turonian active continental margin: Geological Society of America Bulletin, v. 109, p. 1563–1575.

Alavi-Tehrani, N., 1980, Internal report on the Muteh prospects: Geological Survey of Iran (in Persian), Unpublished report, 15 p.

Amman, G., Paar, W.H., Neubauer, F., and Daxner, G., 2002, Auriferous arsenopyrite-pyrite and stibnite mineralization from the Siflitz-Guginock area (Austria): Indications for hydrothermal activity during Tertiary oblique terrane accretion in the Eastern Alps: Geological Society of London Special Publication 204, p. 103–117.

Asadi, H.H., Voncken, J.H.L., Kühnel, R.A., and Hale, M., 2000, Petrography, mineralogy and geochemistry of the Zarshuran Carlin-like gold deposit, northwest Iran: Mineralium Deposita, v. 35, p. 656–671.

Ashley, R.P., 1991, Gold and silver deposits of the United States: Geological Society of America, The Geology of North America, v. P-2, p. 3–21.

Baharifar, A., Moinevaziri, H., Bellon, H., and Piqué, A., 2004, The crystalline complexes of Hamadan (Sanadaj-Sirjan zone, western Iran): Metasedimentary Mesozoic sequences affected by Late Cretaceous tectono-metamorphic and plutonic events: Comptes rendus Geoscience, v. 336, p. 1443–1452.

Baker, T., 2002, Emplacement depth and carbon dioxide-rich fluid inclusions in intrusion-related gold deposits: ECONOMIC GEOLOGY, v. 97, p. 1111–1117.

Bazin, D., and Hübner, H., 1969a, La région cuprifère à gisements porphyriques de Kerman (Iran): Mineralium Deposita, v. 4, p. 200–212.

——1969b, Copper deposits in Iran: Geological Survey of Iran Report 13, 195 p.

Beaudoin, G., Taylor, B.E., and Sangster, D.F., 1991, Silver-lead-zinc veins, metamorphic core complexes, and hydraulic regimes during crustal extension: Geology, v. 19, p. 1217–1220.

Bennett, D.G., and Barker, A.J., 1992, High salinity fluids: the result of retrograde metamorphism in thrust zones: Geochimica et Cosmochimica Acta, v. 56, 81–95.

Berberian, F., and Berberian, M., 1981, Tectono-plutonic episodes in Iran: American Geophysical Union, Geodynamic Series, v. 3, p. 5–32.

Berberian, M., and King, G.C.P., 1981, Towards a paleogeography and tectonic evolution of Iran: Canadian Journal of Earth Sciences, v. 18, p. 210–265.

Berberian, F., Muir, I.D., Pankhurst, R.J., and Berberian, M., 1982, Late Cretaceous and early Miocene Andean-type plutonic activity in northern Makran and Central Iran: Journal of the Geological Society of London, v. 139, p. 605–614.

Bodnar, R.J., 2003, Introduction to aqueous-electrolyte fluid inclusions: Mineralogical Association of Canada Short Course 32, p. 81–100.

Bonev, N., Burg, J.-P., and Ivanov, Z., 2006, Mesozoic-Tertiary structural evolution of an extensional gneiss dome—the Kesebir-Kardamos dome, Eastern Rhodope (Bulgaria-Greece): International Journal of Earth Science, v. 95, p. 318–340.

Boullier, A.-M., France-Lanord, C., Dubessy, J., Adamy, J., and Champenois, M., 1991, Linked fluid and tectonic evolution in the high Himalaya mountains (Nepal): Contributions to Mineralogy and Petrology, v. 107, 358–372.

Braud, J., 1987, La suture du Zagros au niveau de Kermanshah (Kurdistan iranien): Reconstitution palégéographique, évolution géodynamique, magmatique et structurale: Unpublished Ph. D. thesis, Université de Paris-Sud, 489 p.

Braud, J., and Ricou, L.-E., 1971, L'accident du Zagros ou Main Thrust, un charriage et un coulissement: Comptes Rendus de l'Académie des Sciences de Paris, v. 272, p. 203–206.

Cassard, D., Feybesse, J.-L., and Lescuyer, J.-L., 1993, Variscan crustal thickening and late overstacking during the Namurian-Westphalian in the western Montagne Noire (France): Tectonophysics, v. 222, p. 33–53.

Cassidy, K.F., and Bennett, J.M., 1993, Gold mineralisation at the Lady Bountiful mine, Western Australia: An example of a granitoid-hosted Archaean lode gold deposit: Mineralium Deposita, v. 28, p. 388–408.

Chauvet, A., and Dallmeyer, R.D., 1992, $^{40}Ar/^{39}Ar$ mineral dates related to Devonian extension in the southwest Scandinavian Caledonides: Tectonophysics, v. 210, p. 155–177.

Chen, H-S., 1972, The thermodynamics and composition of carbon dioxide hydrate: Unpublished M.Sc. thesis, Syracuse, NY, Syracuse University, 68 p.

Collins, P.L.F., 1979, Gas hydrates in $CO_2$-bearing fluid inclusions and the use of freezing data for the estimation of salinity: ECONOMIC GEOLOGY, v. 74, p. 1435–1444.

Crawford, A.R., 1977, A summary of isotopic age data for Iran, Pakistan and India: Société géologique de France, Mémoire hors série n°8, p. 251–260.

Davies, J.H., and von Blanckenburg, F., 1995, Slab breakoff: A model of lithosphere detachment and its test in the magmatism and deformation of collisional orogens: Earth and Planetary Science Letters, v. 129, p. 85–102.

Davis, G.A., 1988, Rapid upward transport of mid-crustal mylonitic gneisses in the footwall of a Miocene detachment fault, Whipple Mountains, southeastern California: Geologische Rundschau, v. 77, p. 191–209.

Davoudzadeh, M., and Weber-Diefenbach, K., 1987, Contribution to the paleogeography, stratigraphy and tectonics of the Upper Paleozoic of Iran: Neues Jahrbuch für Geologie und Paläontologie-Abhandlungen, v. 175, p. 121–146.

Davoudzadeh, M., Lensch, G., and Weber-Diefenbach, K., 1986, Contribution to the paleogeography, stratigraphy and tectonics of the Infracambrian and lower Paleozoic of Iran: Neues Jahrbuch für Geologie und Paläontologie-Abhandlungen, v. 172, p. 245–269.

De Boorder, H., Spakman, W., White, S.H., and Wortel, M.J.R., 1998, Late Cenozoic mineralization, orogenic collapse and slab detachment in the European Alpine belt: Earth and Planetary Science Letters, v. 164, p. 569–575.

Diamond, L.W., 1992, Stability of $CO_2$ clathrate hydrate + $CO_2$ liquid + $CO_2$ vapour + aqueous KCl-NaCl solutions: Experimental determinations and application to salinity estimates of fluid inclusions: Geochimica et Cosmochimica Acta, v. 56, p. 273–280.

Echtler, H., and Malavieille, J., 1990, Extensional tectonics, basement uplift and Stephano-Permian collapse basin in a late Variscan metamorphic core complex (Montagne Noire, Southern Massif Central): Tectonophysics, v. 177, p. 125–138.

Farhangi, A., 1991, Gold prospecting in Muteh region, Esfahan, Iran, *in* Ladeira, E.A., ed., Brazil Gold '91: Rotterdam, Balkema, p. 801–804.

Faryad, S.W., 2002, Metamorphic conditions and fluid compositions of scapolite-bearing rocks from the lapis lazuli deposit at Sre Sang, Afghanistan: Journal of Petrology, v. 43, p. 725–747.

Förster, H., 1974, Magmentypen und Erzlagerstätten im Iran: Geologische Rundschau, v. 63, p. 276–292.

——1978, Mesozoic-Cenozoic metallogenesis in Iran: Journal of the Geological Society of London, v. 135, p. 443–455.

Friedmann, S.J., and Burbank, D.W., 1995, Rift basins and supradetachment basins—intracontinental extensional end members: Basin Research, v. 7, p. 109–127.

Ghasemi, A., and Talbot, C.J., 2006, A new tectonic scenario for the Sanandaj-Sirjan zone (Iran): Journal of Asian Earth Sciences, v. 26, p. 683–693.

Gilg, H.A., Boni, M., Balassone, G., Allen, C.R., Banks, D., and Moore, F., 2006, Marble-hosted sulfide ores in the Angouran Zn-(Pb-Ag) deposit, NW Iran: Interaction of sedimentary brines with a metamorphic core complex: Mineralium Deposita, v. 41, p. 1–16.

Giuliani, G., Cheilletz, A., Arboleda, C., Carillo, V., Rueda, F., and Baker, J., 1995, An evaporitic origin of the parent brines of the Colombian emeralds: Fluid inclusions and sulfur isotopes evidence: European Journal of Mineralogy, v. 7, p. 151–165.

Goldfarb, R.J., Baker, T., Dubé, B., Groves, D.I., Hart, C.J.R., and Gosselin, P., 2005, Distribution, character, and genesis of gold deposits in metamorphic terranes: ECONOMIC GEOLOGY 100TH ANNIVERSARY VOLUME, p. 407–450.

Groves, D.I., Goldfarb, R.J., Robert, F., and Hart, C.J.R., 2003, Gold deposits in metamorphic belts: Overview of current understanding, outstanding problems, future research, and exploration significance: ECONOMIC GEOLOGY, v. 98, p. 1–29.

Hanes, J.A., 1991, K-Ar and 40Ar/39Ar geochronology: Methods and applications: Mineralogical Association of Canada Short Course 19, p. 27–57.

Hedenquist, J.W., and Henley, R.W., 1985, The importance of $CO_2$ on freezing point measurements of fluid inclusions: Evidence from active geothermal systems and implications for epithermal ore deposition: ECONOMIC GEOLOGY, v. 80, p. 1379–1406.

Heidari, S.M., Rastad, E., Mohajjel, M., and Shamsa, S.M.J., 2006, Gold mineralization in ductile shear zone of Kervian (southwest of Saqez-Kordestan province): Geosciences, v. 58, p. 18–37 (in Persian with English abs.).

Hezarkhani, A., and Williams-Jones, A.E., 1998, Controls of alteration and mineralization in the Sungun porphyry copper deposit, Iran: Evidence from fluid inclusions and stable isotopes: ECONOMIC GEOLOGY, v. 93, p. 651–670.

Hodges, K.V., Walker, J.D., and Wernicke, B.P., 1987, Footwall structural evolution on the Tucki detachment system, Death valley region, southeastern California: Geological Society of London Special Publication 28, p. 393–408.

Hodges, K.V., Parrish, R.R., and Searle, M.P., 1996, Tectonic evolution of the central Annapurna range, Nepalese Himalayas: Tectonics, v. 15, p. 1264–1291.

Hooper, R.J., Baron, I., Hatcher Jr., R.D., and Agah, S., 1994, The development of the southern Tethyan margin in Iran after the break-up of Gondwana—implications for the Zagros hydrocarbon province: Geosciences Iran, v. 4, p. 72–85.

Horner, J., Neubauer, F., Paar, W.H., Hansmann, W., Koeppel, V., and Robl, K., 1997, Structure, mineralogy, and Pb isotopic composition of the As-Au-Ag deposit Rotgülden, eastern Alps (Austria): Significance for formation of epigenetic ore deposits within metamorphic domes: Mineralium Deposita, v. 32, p. 555–568.

Jankovic, S., 1977, The copper deposits and geotectonic setting of the Tethyan Eurasian metallogenic belt: Mineralium Deposita, v. 12, p. 37–47.
——1997, The Carpatho-Balkanides and adjacent area: A sector of the Tethyan Eurasian metallogenic belt: Mineralium Deposita, v. 32, p. 426–433.

Karimzadeh Somarin, A., and Moayyed, M., 2002, Granite- and gabbrodiorite-associated skarn deposits of NW Iran: Ore Geology Reviews, v. 20, p. 127–138.

Kelley, S., 2002, Excess argon in K-Ar and Ar-Ar geochronology: Chemical Geology, v. 188, p. 1–22.

Kelley, S.P., Arnaud, N.O., and Turner, S.P., 1994, High spatial resolution 40Ar/39Ar investigations using an ultra-violet laser probe extraction technique: Geochimica et Cosmochimica Acta, v. 58, p. 3519–3525.

Kouhestani, H., 2005, Geology, mineralogy, geochemistry and fabrics of gold mineralization in Chah-Bagh shear zones at Muteh mining area (southwest of Delijan, Esfahan province): Unpublished M.Sc. thesis, Tehran, Iran, University of Tarbiat-Modarres, 222 p. (in Persian).

Kouhestani, H., Rastad, E., Rasidnejad, N., and Mohajjel, M., 2005, The role of deformation and alteration in gold mineralization in Chah-Bagh deposit shear zones [abs.]: Geological Survey of Iran, Geology Symposium, 23rd, Tehran, Iran, p. 50–51 (Persian and English abs.).

Kwak, T.A.P., 1977, Scapolite compositional change in a metamorphic gradient and its bearing on the identification of meta-evaporite sequences: Geological Magazine, v. 114, p. 343–354.

Lang, J.R., and Baker, T., 2001, Intrusion-related gold systems: the present level of understanding: Mineralium Deposita, v. 36, p. 477–489.

Lee, J., Miller, E.L., and Sutter, S.F., 1987, Ductile strain and metamorphism in an extensional tectonic setting: A case study from the northern Snake range, Nevada, USA: Geological Society of London Special Publication 28, p. 267–298.

Lescuyer, J.L., Hushmand Zadeh, A., and Daliran, F., 2003, Gold metallogeny in Iran: a preliminary review, in Eliopoulos, D.G. et al.., eds., Mineral exploration and sustainable developement: Rotterdam, Netherlands, Millpress, v. 2, p. 1185–1188.

Leterrier, J., 1985, Mineralogical, geochemical and isotopic evolution of two Miocene mafic intrusions from the Zagros (Iran): Lithos, v. 18, p. 311–329.

Lister, G.S., and Davis, G.A., 1989, The origin of metamorphic core complexes and detachment faults formed during Tertiary continental extension in the northern Colorado River region, U.S.A.: Journal of Structural Geology, v. 11, p. 65–94.

Lo, C.H., and Onstott, T.C., 1989, 39Ar recoil artifacts in chloritized biotite: Geochimica et Cosmochimica Acta, v. 53, p. 2697–2711.

Long, K.L., 1992, Preliminary descriptive deposit model for detachment fault-related mineralization: U.S. Geological Survey Bulletin, v. 2004, p. 52–62.

Losh, S., Purvance, D., Sherlock, R., and Jowett, E.C., 2005, Geologic and geochemical study of the Picacho gold mine, California: Gold in a low-angle normal fault environment: Mineralium Deposita, v. 40, p. 137–155.

Mahood, G.A., and Drake, R.E., 1982, K-Ar dating young rhyolitic rocks: A case study of the Sierra La Primavera, Mexico: Geological Society of America Bulletin, v. 93, p. 1232–1241.

Marchev, P., Singer, B., Jelev, D, Hasson, S., Moritz, R., and Bonev, N., 2004, The Ada Tepe deposit: An example of a sedimentary-hosted and detachment fault-controlled low-sulfidation gold mineralization in the eastern Rhodopes, SE Bulgaria: Swiss Bulletin of Mineralogy and Petrology, v. 84, p. 59–78.

Marton, I., Moritz, R., Marchev, P., Vennemann, T., and Spangenberg, J.E., 2006, Fluid evolution within eastern Rhodopian sedimentary rock-hosted low-sulfidation epithermal gold deposits, Bulgaria: IGCP 486 project, Izmir, Turkey, 24–29 Sepetember 2006, Proceedings of the 2006 field workshop, p. 116–123.

McDougall, I., and Harrison, T.M., 1999, Geochronology and thermochronology by the 40Ar/39Ar method: Oxford University Press, 2nd ed., 288 p.

Mehrabi, B., Yardley, B.W.D., and Cann, J.R., 1999, Sediment-hosted disseminated gold mineralisation at Zarshuran, NW Iran: Mineralium Deposita, v. 34, p. 673–696.

Mikucki, E.J., and Ridley, J.R., 1993, The hydrothermal fluid of Archaean lode-gold deposits at different metamorphic grades: Compositional constraints from ore and wallrock alteration assemblages: Mineralium Deposita, v. 28, p. 469–481.

Miller, E.L., Gans, P.B., and Garing, J., 1983, The Snake Range décollement: An exhumed mid-Tertiary ductile-brittle transition: Tectonics, v. 2, p. 239–263.

Mohajjel M., and Fergusson, C.L., 2000, Dextral transpression in Late Cretaceous continental collision, Sanandaj-Sirjan zone, western Iran: Journal of Structural Geology, v. 22, p. 1125–1139.

Mohajjel, M., Fergusson, C.L., and Sahandoi, M.R., 2003, Cretaceous-Tertiary convergence and continental collision, Sanandaj-Sirjan zone, western Iran: Journal of Asian Earth Sciences, v. 21, p. 397–412.

Moine, B., Sauvan, P., and Jarousse, J., 1981, Geochemistry of evaporite-bearing series: A tentative guide for the identification of metaevaporites: Contribution to Mineralogy and Petrology, v. 76, p. 401–412.

Momenzadeh, M., 1979, Internal report on the Muteh prospects: Geological Survey of Iran Unpublished report, 27 p. (in Persian).

Mora, C.I., and Valley, J.W., 1989, Halogen-rich scapolite and biotite—implications for metamorphic fluid rock interaction: American Mineralogist, v. 74, p. 721–37.

Nabelek, P.I., and Ternes, K., 1997, Fluid inclusions in the Harney Peak Granite, Black Hills, South Dakota, USA: Implications for solubility and evolution of magmatic volatiles and crystallization of leucogranite magmas: Geochimica et Cosmochimica Acta, v. 61, p. 1447–1465.

Neubauer, F., Dallmeyer, R.D., Dunkl, I., and Schirnik, D., 1995, Late Cretaceous exhumation of the metamorphic Gleinalm dome, Eastern Alps: Kinematics, cooling history and sedimentary response in a sinistral wrench corridor: Tectonophysics, v. 242, p. 79–98.

Oliver, N.H.S., Wall, V.J., and Cartwright, I., 1992, Internal control of fluid compositions in amphibolite-facies scapolitic calc-silicates, Mary-Kathleen, Australia: Contributions to Mineralogy and Petrology, v. 111, p. 94–112.

Paidar-Saravi, H., 1989, Petrographisch-lagerstättenkundliche Untersuchungen an goldführenden Gesteinen im Muteh-Gebiet im Westen vom Zentraliran: Heidelberger Geowissenschaftliche Abhandlungen, v. 33, 174 p.

Passchier, C.W., and Trouw, R.A.J., 1998, Microtectonics: Berlin, Springer-Verlag, 289 p.

Rachidnejad-Omran N., Emami, M.H., Sabzehei, M., Rastad, E., Bellon, H., and Piqué, A., 2002 Lithostratigraphie et histoire paléozoïque à paléocène des complexes métamorphiques de la région de Muteh, zone de Sanandaj-Sirjan (Iran méridional): Comptes rendus Geoscience, v. 334, p. 1185–1191.

Renne, P.R., 1995, Excess 40Ar in biotite and hornblende from the Noril'sk 1 intrusion, Siberia: Implications for the age of the Siberian traps: Earth and Planetary Science Letters, v. 131, p. 165–176.

Renne, P.R., Swisher, C.C., Deino, A.L., Karner, D.B., Owens, T.L., and De-Paolo, D.J., 1998, Intercalibration of standards, absolute ages and uncertainties in $^{40}$Ar/$^{39}$Ar dating: Chemical Geology, v. 145, p. 117–152.

Rich, R.A., 1979, Fluid inclusion evidence for Silurian evaporites in southeastern Vermont: Summary: Geological Society of America Bulletin, v. 90, p. 901–902.

Richards, J.P., and Noble, S.R., 1998, Applications of radiogenic isotope systems to the timing and origin of hydrothermal processes: Reviews in Economic Geology, v. 10, p. 195–233.

Ridley, J.R., and Diamond, L.W., 2000, Fluid chemistry of orogenic lode gold deposits and implications for genetic models: Reviews in Economic Geology, v. 13, p. 141–162.

Ring, U., Brandon, M.T., Willet, S.D., and Lister, G.S., 1999, Exhumation processes: Geological Society of London Special Publication 154, p. 1–27.

Roddick, J.C., Cliff, R.A., and Rex, D.C., 1980, The evolution of excess argon in Alpine biotites—a $^{40}$Ar-$^{39}$Ar analysis: Earth and Planetary Science Letters, v. 48, p. 185–208.

Roddy, M.S., Reynolds, S.J., Smith, B.M., and Ruiz, J., 1988, K-metasomatism and detachment-related mineralization, Harcuvar Mountains, Arizona: Geological Society of America Bulletin, v. 100, p. 1627–1639.

Samani, B.A., 1988, Metallogeny of the Precambrian in Iran: Precambrian Research, v. 39, p. 85–106.

Schoonover, M., and Osozawa, S., 2004, Exhumation process of the Nago subduction-related metamorphic rocks, Okinawa, Ryuku island arc: Tectonophysics, v. 393, p. 221–240.

Schröder, J.W., 1944, Essai sur la structure de l'Iran: Eclogae Geologicae Helvetiae, v. 37, p. 37–81.

Searle, M.P., 1999, Extensional and compressional faults in the Everest-Lhotse massif, Khumbu Himalaya, Nepal: Journal of the Geological Society of London, v. 156, p. 227–240.

Seidel, M., Pack, A., Sharp, Z.D., and Seidel, E., 2005, The Kakopetros and Ravdouche iron oxide deposits, Western Crete, Greece: Fluid transport and mineralization within a detachment zone: ECONOMIC GEOLOGY, v. 100, p. 165–174.

Selverstone, J., 1988, Evidence for east-west crustal extension in the eastern Alps: Implications for the unroofing history of the Tauern window: Tectonics, v. 7, p. 87–105.

Shamanian, G.H., Hedenquist, J.W., Hattori, K.H., and Hassanzadeh, J., 2004, The Gandy and Abolhassani epithermal prospects in the Alborz magmatic arc, Semnan province, northern Iran: ECONOMIC GEOLOGY, v. 99, p. 691–712.

Sheikholeslami, R., Bellon, H., Emami, H., Sabzehei, M., and Piqué, A., 2003, Nouvelles données structurales et datations K-Ar sur les roches métamorphiques de la région de Neyriz (zone de Sanandaj-Sirjan, Iran méridional). Leur intérêt dans le cadre du domaine néo-téthysien du Moyen-Orient: Comptes rendus Geoscience, v. 335, p. 981–991.

Shmulovich, K.I., Tkachenko, S.I., and Plyasunova, N.V., 1994, Phase equilibria in fluid systems at high pressures and temperatures, *in* Shmulovich, K.I., Yardley, B.W.D., and Gonchar, G.G., eds., Fluids in the crust: Equilibrium and transport properties: London, Chapman and Hall, p. 193–214.

Singer, B.S., and Pringle, M.S., 1996, Age and duration of the Matuyama-Brunhes geomagnetic polarity reversal from $^{40}$Ar/$^{39}$Ar incremental-heating analyses of lavas: Earth and Planetary Science Letters, v. 139, p. 47–61.

Singer, B.S., Hoffman, K.A., Chauvin, A., Coe, R.S., and Pringle, M.S., 1999, Dating transitionally magnetized lavas of the late Matuyama Chron: Toward a new $^{40}$Ar/$^{39}$Ar timescale of reversals and events: Journal of Geophysical Research, v. 104, p. 679–693.

Sisson, V.B., Crawford, M.L., and Thompson, P.H., 1981, $CO_2$–brine immiscibility at high temperatures, evidence from calcareous metasedimentary rocks: Contributions to Mineralogy and Petrology, v. 78, p. 371–378.

Spencer, J.E, and Welty, J.W., 1986, Possible controls of base- and precious-metal mineralization associated with Tertiary detachment faults in the lower Colorado River trough, Arizona and California: Geology, v. 14, p. 195–198.

Steiger, R.H., and Jäger, E., 1977, Subcommisssion on geochronology: Convention on the use of decay constants in geo-and cosmochronology: Earth and Planetary Science Letters, v. 36, p. 359–362.

Sterner, S.M., and Bodnar, R.J., 1984, Synthetic fluid inclusions in natural quartz I. Compositional types synthesized and applications to experimental geochemistry: Geochimica et Cosmochimica Acta, v. 48, p. 2659–2668.

Stöcklin, J., 1968, Structural history and tectonics of Iran: A review: American Association of Petroleum Geologists Bulletin, v. 52, p. 1229–1258.

——1974, Possible ancient continental margins in Iran, *in* Bark, G.D., and Drake, C.L., eds., Geology of continental margins: New York, Springer Verlag, p. 873–887.

Teyssier, C., and Whitney, D., 2002, Gneiss domes and orogeny: Geology, v. 30, p. 1139–1142.

Thiele, O., 1966, Zum Alter der Metamorphose in Zentraliran: Mitteilungen der geologischen Gesellschaft [Wien], v. 58, p. 87–101.

Thiele, O., Alavi, M., Assefi, R., Hushmand-zadeh, A., Seyed-Emami, K., and Zahedi, M., 1968, Explanatory text of the Golpaygan quadrangle map 1:250,000: Geological Survey of Iran, Geological Quadrangle E7, 24 p.

Tillman, J.E., Poosti, A., Rossello, S., and Eckert, A., 1981, Structural evolution of Sanandaj-Sirjan Ranges near Esfahan, Iran: American Association of Petroleum Geologists Bulletin, v. 65, p. 674–687.

Touret, J.L.R., 1981, Fluid inclusions in high grade metamorphic rocks: Mineralogical Association of Canada Short Course 6, p. 182–208.

——1985, Fluid regime in southern Norway: the record of fluid inclusions, *in* Tobi, A.C., and Touret, J.L.R., eds., The deep Proterozoic crust in the North Atlantic provinces: Dordrecht, Riedel, p. 445–454.

Trommsdorf, V., Skippen, G., and Ulmer, P., 1985, Halite and sylvite solid inclusions in high-grade rocks: Contributions to Mineralogy and Petrology, v. 89, p. 24–29.

Valizadeh, M.-V., and Cantagrel, J.-M., 1975, Premières données radiométriques (K/Ar et Rb/Sr) sur les micas du complexe magmatique du Mont Alvand, près Hamadan (Iran occidental): Comptes Rendus de l'Académie des Sciences de Paris, v. 281, p. 1083–1086.

Vityk, M.O., and Bodnar, R.J., 1995, Textural evolution of synthetic fluid inclusions in quartz during reequilibration, with applications to tectonic reconstruction: Contributions to Mineralogy and Petrology, v. 121, p. 309–323.

Waterman, G.C., and Hamilton, R.L., 1975, The Sar Cheshmeh porphyry copper deposit: ECONOMIC GEOLOGY, v. 70, p. 568–576.

Wernicke, B., and Burchfiel, B.C., 1982, Modes of extensional tectonics: Journal of Structural Geology, v. 4, p. 105–115.

Werre, R.W., Jr., Bodnar, R.J., Bethke, P.M., and Barton, P.B., Jr., 1979, A novel gas-flow fluid inclusion heating-freezing stage [abs.]: Geological Society of America Abstracts with Programs, v. 11, p. 539.

Wertime, T.A., 1968, A metallurgical expedition through the Persian desert: Science, v. 159, p. 927–935.

West, D.P., Jr., and Lux, D.R., 1993, Dating mylonitic deformation by the $^{40}$Ar-$^{39}$Ar method: An example from the Norumbega fault zone, Maine: Earth and Planetary Science Letters, v. 120, p. 221–237.

Woods, T.L., Bethke, P.M., Bodnar, R.J., and Werre, R.W., Jr., 1981, Supplementary components and operation of the U.S. Geological Survey gas-flow heating/freezing stage: U.S. Geological Survey Open-File Report 81–954, 12 p.

Yardley, B.W.D., and Bottrell, S.H., 1988, Immiscible fluids in metamorphism: Implications of two-phase flow for reaction history: Geology, v. 16, p. 199–202.

Yardley, B.W.D., and Graham, J.T., 2002, The origins of salinity in metamorphic fluids: Geofluids, v. 2, p. 249–256.

Yardley, B.W.D., and Valley, J.W., 1997, The petrologic case for a dry lower crust: Journal of Geophysical Research, v. 102, p. 12173–12185.

Yigit, O., 2006, Gold in Turkey—a missing link in Tethyan metallogeny: Ore Geology Reviews, v. 28, p. 147–179.

APPENDIX 1. $^{40}$Ar/$^{39}$Ar Incremental-Heating Analyses of Biotite, Amphibole, and Muscovite Samples from the Muteh Gold Deposit Area

Sample BH-14/35.40 muscovite      J value: 0.00453

| Laser power (%) | $^{40}$Ar/$^{39}$Ar | $^{37}$Ar/$^{39}$Ar[1] | $^{36}$Ar/$^{39}$Ar | $^{40}$Ar[2] (10$^{-14}$ mol) | $^{40}$Ar[2] (%) | K/Ca | $^{39}$Ar (%) | Apparent age[3] (±2σ Ma) |
|---|---|---|---|---|---|---|---|---|
| 2.2 | 275.80 | 3.28649 | 0.901914 | 0.016 | 3.46 | 14.88 | 2.35 | 21.80 ± 100.15 |
| 2.4 | 302.83 | 3.60635 | 0.989130 | 0.007 | 3.57 | 13.55 | 0.90 | 24.71 ± 185.00 |
| 2.5 | 319.25 | 8.00864 | 1.018258 | 0.037 | 5.95 | 6.09 | 2.70 | 43.24 ± 52.18 |
| 2.6 | 298.23 | 9.16413 | 0.946684 | 0.156 | 6.44 | 5.31 | 8.32 | 43.77 ± 28.08 |
| 2.7 | 361.50 | 8.39556 | 1.149587 | 0.117 | 6.21 | 5.80 | 7.21 | 51.03 ± 36.54 |
| 2.9 | 361.04 | 0.95203 | 1.140286 | 0.125 | 6.69 | 51.44 | 7.19 | 54.60 ± 44.40 |
| 3.0 | 290.86 | 0.40364 | 0.904094 | 0.342 | 8.16 | 121.36 | 20.04 | 53.63 ± 14.26 |
| 3.1 | 234.82 | 0.24739 | 0.721004 | 0.229 | 9.28 | 198.03 | 14.65 | 49.28 ± 17.40 |
| 3.3 | 196.54 | 0.26365 | 0.585135 | 0.182 | 12.03 | 185.82 | 10.72 | 53.44 ± 17.44 |
| 3.4 | 187.75 | 0.27359 | 0.565718 | 0.139 | 10.97 | 179.06 | 9.36 | 46.64 ± 11.66 |
| 3.5 | 221.37 | 0.28118 | 0.681956 | 0.081 | 8.98 | 174.24 | 5.70 | 45.01 ± 33.56 |
| 3.6 | 319.97 | 0.53787 | 1.012299 | 0.091 | 6.52 | 91.07 | 6.07 | 47.26 ± 31.10 |
| 3.7 | 1265 | 5.20124 | 4.177742 | 0.073 | 2.45 | 9.39 | 3.24 | 70.09 ± 272.44 |
| 3.8 | 651.41 | 6.29720 | 1.959667 | 0.082 | 11.18 | 7.75 | 1.55 | 160.41 ± 460.30 |

Weighted mean plateau age (98.4% of total $^{39}$Ar released):    49.3 ± 6.4
Isochron age of the plateau steps:    46.5 ± 8.0
$^{40}$Ar/$^{36}$Ar intercept of the isochron: 296.9 ± 2.2, sums/($n$ = 2) = 0.87

Sample MU-104 amphibole      J value: 0.00443

| Laser power (%) | $^{40}$Ar/$^{39}$Ar | $^{37}$Ar/$^{39}$Ar[1] | $^{36}$Ar/$^{39}$Ar | $^{40}$Ar[2] (10$^{-14}$ mol) | $^{40}$Ar[2] (%) | K/Ca | $^{39}$Ar (%) | Apparent age[3] (±2σ Ma) |
|---|---|---|---|---|---|---|---|---|
| 3.0 | 18.627 | 3.40057 | 0.0194858 | 3.361 | 70.51 | 0.1438 | 10.71 | 103.77 ± 1.40[4] |
| 3.8 | 14.976 | 8.61037 | 0.0076122 | 4.489 | 89.46 | 0.0566 | 13.97 | 106.17 ± 1.44[4] |
| 4.5 | 15.132 | 9.42140 | 0.0063787 | 8.698 | 92.40 | 0.0517 | 25.93 | 110.72 ± 1.38 |
| 5.0 | 14.856 | 9.56438 | 0.0062143 | 8.047 | 92.66 | 0.0509 | 24.37 | 109.07 ± 1.26 |
| 5.3 | 14.782 | 9.20776 | 0.0061863 | 7.286 | 92.49 | 0.0529 | 22.22 | 108.32 ± 1.12 |
| 5.5 | 15.793 | 9.14186 | 0.0088630 | 0.722 | 87.93 | 0.0533 | 2.17 | 109.98 ± 4.34 |
| 6.5 | 16.455 | 10.41947 | 0.0011389 | 0.211 | 84.48 | 0.0467 | 0.63 | 110.18 ± 14.32 |

Weighted mean plateau age (75.3% of total $^{39}$Ar released):    109.65 ± 2.04
Isochron age of the plateau steps:    106.54 ± 5.64
$^{40}$Ar/$^{36}$Ar intercept of the isochron: 368.5 ± 115.3, sums/($n$ = 2) = 0.72

Sample MU-104 biotite      J value: 0.00448

| Laser power (%) | $^{40}$Ar/$^{39}$Ar | $^{37}$Ar/$^{39}$Ar[1] | $^{36}$Ar/$^{39}$Ar | $^{40}$Ar[2] (10$^{-14}$ mol) | $^{40}$Ar[2] (%) | K/Ca | $^{39}$Ar (%) | Apparent age[3] (±2σ Ma) |
|---|---|---|---|---|---|---|---|---|
| 2.3 | 11.683 | 0.01110 | 0.0036840 | 3.587 | 90.68 | 44.16 | 7.68 | 84.91 ± 1.08[4] |
| 2.5 | 11.487 | 0.00832 | 0.0023608 | 7.916 | 93.92 | 58.90 | 16.64 | 86.43 ± 0.82 |
| 2.7 | 11.461 | 0.01721 | 0.0022031 | 5.650 | 94.32 | 28.48 | 11.85 | 86.60 ± 0.86 |
| 2.9 | 11.397 | 0.01904 | 0.0021752 | 7.270 | 94.37 | 25.74 | 15.33 | 86.16 ± 0.86 |
| 3.1 | 11.383 | 0.02078 | 0.0018558 | 5.030 | 95.19 | 23.58 | 10.53 | 86.80 ± 1.06 |
| 3.3 | 11.296 | 0.02439 | 0.0019351 | 4.986 | 94.95 | 20.09 | 10.54 | 85.94 ± 1.22 |
| 3.5 | 11.347 | 0.03701 | 0.0018027 | 5.279 | 95.32 | 13.24 | 11.07 | 86.64 ± 1.04 |
| 3.8 | 11.377 | 0.04194 | 0.0018899 | 2.560 | 95.11 | 11.68 | 5.37 | 86.68 ± 1.70 |
| 4.1 | 11.562 | 0.04754 | 0.0023117 | 1.481 | 94.12 | 10.31 | 3.09 | 87.16 ± 2.28 |
| 4.6 | 11.748 | 0.03955 | 0.0024402 | 1.613 | 93.88 | 12.39 | 3.32 | 88.32 ± 1.94[4] |
| 5.6 | 11.613 | 0.04855 | 0.0019305 | 2.235 | 95.11 | 10.09 | 4.59 | 88.44 ± 1.26[4] |

Weighted mean plateau age (84.4% of total $^{39}$Ar released):    86.55 ± 1.00
Isochron age of the plateau steps:    85.82 ± 2.36
$^{40}$Ar/$^{36}$Ar intercept of the isochron: 326.5 ± 96.0, sums/(n-2) = 0.60

Sample MU-361 biotite      J value: 0.004401

| Laser power (%) | $^{40}$Ar/$^{39}$Ar | $^{37}$Ar/$^{39}$Ar[1] | $^{36}$Ar/$^{39}$Ar | $^{40}$Ar[2] (10$^{-14}$ mol) | $^{40}$Ar[2] (%) | K/Ca | $^{39}$Ar (%) | Apparent age[3] (±2σ Ma) |
|---|---|---|---|---|---|---|---|---|
| 3.0 | 9.665 | 0.00338 | 0.0018221 | 6.145 | 94.42 | 144.98 | 37.96 | 72.11 ± 0.72 |
| 3.3 | 9.527 | 0.00392 | 0.0014322 | 3.009 | 95.55 | 124.94 | 18.64 | 71.93 ± 0.84 |
| 3.5 | 9.379 | 0.00358 | 0.0009790 | 2.632 | 96.91 | 137.04 | 16.33 | 71.82 ± 0.90 |
| 3.9 | 9.349 | 0.00492 | 0.0012552 | 2.136 | 96.03 | 99.58 | 13.41 | 70.96 ± 0.84 |
| 4.3 | 9.442 | 0.00257 | 0.0011170 | 1.739 | 96.50 | 190.63 | 10.76 | 71.98 ± 1.20 |
| 4.6 | 11.597 | 0.001738 | 0.0118672 | 1.598 | 69.76 | 281.91 | 1.79 | 70.22 ± 10.16 |
| 5.0 | 9.978 | 0.003556 | 0.0037038 | 0.281 | 89.02 | 1.00 | 1.11 | 64.06 ± 5.24 |

Weighted mean plateau age (100% of total $^{39}$Ar released):    71.83 ± 0.62
Isochron age of the plateau steps:    71.33 ± 1.52
$^{40}$Ar/$^{36}$Ar intercept of the isochron: 339.6 ± 64.9, sums/(n-2) = 1.64

APPENDIX 1. *(Cont.)*

Sample MU-407a biotite    J value: 0.004535

| Laser power (%) | $^{40}Ar/^{39}Ar$ | $^{37}Ar/^{39}Ar^1$ | $^{36}Ar/^{39}Ar$ | $^{40}Ar^2$ ($10^{-14}$ mol) | $^{40}Ar^2$ (%) | K/Ca | $^{39}Ar$ (%) | Apparent age[3] (±2σ Ma) |
|---|---|---|---|---|---|---|---|---|
| 2.4 | 9.341 | 0.00759 | 0.0015672 | 0.672 | 95.04 | 65.08 | 1.22 | 70.01 ± 2.10[4] |
| 2.6 | 9.423 | 0.00470 | 0.0010154 | 3.492 | 96.81 | 104.15 | 6.15 | 71.90 ± 0.86[4] |
| 2.9 | 9.439 | 0.00396 | 0.0009558 | 5.041 | 97.00 | 123.85 | 8.85 | 72.16 ± 0.68[4] |
| 3.1 | 9.443 | 0.00440 | 0.0006166 | 7.083 | 98.07 | 111.46 | 12.30 | 72.96 ± 0.66[4] |
| 3.3 | 9.478 | 0.00226 | 0.0002406 | 3.982 | 99.24 | 216.54 | 6.81 | 74.08 ± 0.76[4] |
| 3.4 | 9.462 | 0.00383 | 0.0003370 | 3.476 | 98.94 | 127.81 | 5.97 | 73.75 ± 0.70 |
| 3.6 | 9.396 | 0.00325 | 0.0003565 | 7.013 | 98.87 | 150.91 | 12.14 | 73.19 ± 0.68 |
| 3.9 | 9.355 | 0.00309 | 0.0003793 | 7.981 | 98.80 | 158.53 | 13.88 | 72.83 ± 0.64 |
| 4.1 | 9.386 | 0.00131 | 0.0004084 | 5.506 | 98.71 | 372.66 | 9.55 | 73.00 ± 0.68 |
| 4.4 | 9.406 | 0.00154 | 0.0003377 | 6.196 | 98.93 | 317.46 | 10.70 | 73.31 ± 0.64 |
| 4.6 | 9.454 | 0.00146 | 0.0005437 | 2.947 | 98.29 | 334.66 | 5.10 | 73.21 ± 0.80 |
| 4.9 | 9.496 | 0.00046 | 0.0004409 | 2.483 | 98.62 | 1070 | 4.26 | 73.77 ± 0.88 |
| 5.4 | 9.504 | 0.00028 | 0.0000623 | 1.188 | 99.80 | 1749 | 2.01 | 74.69 ± 0.98[4] |
| 6.3 | 9.502 | 0.00053 | 0.0001186 | 0.623 | 99.62 | 918 | 1.06 | 74.55 ± 1.00[4] |

Weighted mean plateau age (61.6% of total $^{39}Ar$ released): 73.21 ± 0.58
Isochron age of the plateau steps: 119.82 ± 65.60
$^{40}Ar/^{36}Ar$ intercept of the isochron: -16347.7 ± 151923.1, sums/(n-2) = 1.22

Sample MU-701 biotite    J value: 0.00444

| Laser power (%) | $^{40}Ar/^{39}Ar$ | $^{37}Ar/^{39}Ar^1$ | $^{36}Ar/^{39}Ar$ | $^{40}Ar^2$ ($10^{-14}$ mol) | $^{40}Ar^2$ (%) | K/Ca | $^{39}Ar$ (%) | Apparent age[3] (±2σ Ma) |
|---|---|---|---|---|---|---|---|---|
| 2.8 | 14.921 | 0.01198 | 0.0046821 | 7.412 | 90.73 | 40.92 | 20.45 | 106.88 ± 1.08 |
| 3.0 | 15.247 | 0.01521 | 0.0046871 | 8.055 | 90.92 | 32.22 | 21.71 | 109.37 ± 1.04 |
| 3.2 | 15.087 | 0.01476 | 0.0046127 | 6.914 | 90.97 | 33.20 | 18.82 | 108.31 ± 1.04 |
| 3.3 | 15.626 | 0.01725 | 0.0043066 | 6.191 | 91.86 | 28.40 | 16.11 | 113.13 ± 0.98[4] |
| 3.5 | 16.088 | 0.01255 | 0.0037038 | 3.697 | 93.20 | 39.04 | 9.21 | 118.01 ± 1.32[4] |
| 3.6 | 16.511 | 0.01779 | 0.0030331 | 2.024 | 94.57 | 27.55 | 4.84 | 122.74 ± 1.74[4] |
| 3.8 | 16.933 | 0.02009 | 0.0027215 | 2.095 | 95.25 | 24.39 | 4.85 | 126.65 ± 1.60[4] |
| 4.1 | 17.290 | 0.04598 | 0.0025835 | 1.192 | 95.60 | 10.66 | 2.69 | 129.69 ± 2.86[4] |
| 4.5 | 17.411 | 0.00285 | 0.0082351 | 0.188 | 86.02 | 171.66 | 0.47 | 117.88 ± 12.08[4] |
| 4.9 | 18.868 | 0.04205 | 0.0024560 | 0.404 | 96.17 | 11.65 | 0.83 | 141.88 ± 6.56[4] |

Weighted mean plateau age (61% of total $^{39}Ar$ released): 108.29 ± 0.92
Isochron age of the plateau steps:
$^{40}Ar/^{36}Ar$ intercept of the isochron: 384.82 ± 21.28, sums/(n = 2) = 5.20

Sample MU-715 amphibole    J value: 0.00446

| Laser power (%) | $^{40}Ar/^{39}Ar$ | $^{37}Ar/^{39}Ar^1$ | $^{36}Ar/^{39}Ar$ | $^{40}Ar^2$ ($10^{-14}$ mol) | $^{40}Ar^2$ (%) | K/Ca | $^{39}Ar$ (%) | Apparent age[3] (±2σ Ma) |
|---|---|---|---|---|---|---|---|---|
| 2.3 | 3346.483 | 4.20875 | 2.761789 | 0.037 | 75.62 | 0.1161 | 0.00 | 4598.05 ± 24926[4] |
| 3.0 | 303.374 | 0.00906 | 0.6873038 | 0.606 | 33.05 | 54.08 | 0.38 | 676.85 ± 86.68[4] |
| 3.6 | 148.650 | 1.18269 | 0.3617988 | 1.173 | 28.14 | 0.4140 | 1.78 | 313.45 ± 31.70[4] |
| 4.0 | 48.964 | 1.15890 | 0.1027843 | 0.845 | 38.22 | 0.3080 | 2.86 | 146.94 ± 9.62[4] |
| 4.3 | 55.562 | 1.77978 | 0.1133361 | 0.712 | 39.97 | 0.2750 | 2.03 | 173.14 ± 10.84[4] |
| 4.6 | 57.483 | 1.82431 | 0.1232687 | 0.740 | 36.88 | 0.2683 | 2.21 | 165.61 ± 15.34[4] |
| 5.1 | 42.275 | 1.79808 | 0.0865252 | 0.574 | 39.85 | 0.2722 | 2.16 | 132.81 ± 13.02[4] |
| 5.6 | 39.327 | 1.80100 | 0.0754715 | 0.630 | 43.65 | 0.2717 | 2.33 | 135.23 ± 10.84[4] |
| 6.0 | 70.310 | 1.75970 | 0.1532828 | 0.817 | 35.77 | 0.2781 | 2.06 | 194.89 ± 19.94[4] |
| 6.5 | 77.904 | 1.64999 | 0.1916706 | 0.551 | 27.46 | 0.2966 | 1.63 | 167.05 ± 15.34[4] |
| 7.0 | 46.806 | 1.63269 | 0.1196121 | 0.166 | 24.76 | 0.2998 | 0.91 | 92.37 ± 18.60[4] |
| 7.8 | 26.860 | 1.44028 | 0.0516273 | 0.177 | 43.62 | 0.3399 | 0.96 | 93.35 ± 12.94[4] |
| 8.5 | 27.924 | 1.09727 | 0.0568015 | 0.226 | 40.19 | 0.4462 | 1.28 | 89.50 ± 14.28[4] |
| 9.3 | 13.670 | 0.52507 | 0.0138236 | 0.324 | 70.41 | 0.9329 | 2.13 | 76.99 ± 5.68[4] |
| 10.0 | 10.910 | 0.38581 | 0.0113314 | 0.260 | 68.22 | 1.2697 | 2.22 | 59.81 ± 6.28 |
| 10.8 | 8.597 | 0.18334 | 0.0045063 | 0.352 | 84.67 | 2.6724 | 3.07 | 58.50 ± 4.78 |
| 11.8 | 8.106 | 0.06036 | 0.0021497 | 0.527 | 92.21 | 8.1183 | 4.47 | 60.05 ± 3.34 |
| 13.0 | 7.819 | 0.03135 | 0.0024531 | 0.690 | 90.75 | 15.63 | 6.17 | 57.04 ± 2.34 |
| 14.3 | 8.225 | 0.03077 | 0.0018810 | 0.959 | 93.26 | 15.93 | 7.93 | 61.60 ± 1.76 |
| 15.5 | 7.944 | 0.03032 | 0.0018728 | 1.068 | 93.05 | 16.16 | 9.16 | 59.39 ± 1.58 |
| 16.5 | 8.005 | 0.03798 | 0.0015736 | 1.136 | 94.22 | 12.90 | 9.55 | 60.59 ± 0.94 |
| 17.5 | 8.068 | 0.03551 | 0.0014750 | 1.171 | 94.62 | 13.80 | 9.73 | 61.31 ± 1.40 |
| 18.5 | 7.985 | 0.01904 | 0.0018745 | 1.169 | 93.07 | 25.73 | 9.98 | 59.71 ± 1.10 |
| 19.5 | 8.111 | 0.01285 | 0.0017626 | 1.139 | 93.58 | 38.12 | 9.52 | 60.96 ± 1.20 |
| 20.5 | 6.135 | 0.01686 | 0.0019847 | 0.480 | 90.45 | 29.07 | 5.49 | 44.76 ± 2.62[4] |

Weighted mean plateau age (71.8% of total $^{39}Ar$ released): 60.35 ± 0.64
Isochron age of the plateau steps: 59.85 ± 1.84
$^{40}Ar/^{36}Ar$ intercept of the isochron: 331.1 ± 67.9, sums/(n = 2) = 2.03

[1] Corrected for $^{37}Ar$ and $^{39}Ar$ decay, half-lives of 35 d and 259 yr, respectively
[2] Radiogenic argon (nonatmospheric argon)
[3] Ages calculated relative to the Taylor Creek rhyolite (28.34 Ma, Renne et al., 1998)
[4] Indicates step not used in plateau age calculation

APPENDIX 2. $^{40}$Ar/$^{39}$Ar Laser-Ablation Analyses of Biotite, Amphibole, and Muscovite Samples from the Muteh Gold Deposit Area

**Sample MU-322 muscovite**      J value: 0.00453

| Experiment no. | $^{40}$Ar/$^{39}$Ar | $^{37}$Ar/$^{39}$Ar[1] | $^{36}$Ar/$^{39}$Ar | $^{40}$Ar[2] ($10^{-14}$ mol) | $^{40}$Ar[2] (%) | K/Ca | Apparent age[3] (±2σ Ma) |
|---|---|---|---|---|---|---|---|
| GE9D209A | 6.631 | 0.21882 | 0.0043919 | 0.139 | 80.67 | 2.24 | 43.85 ± 9.62 |
| GE9D209B | 6.474 | 0.20981 | 0.0005499 | 0.123 | 97.73 | 2.34 | 51.75 ± 11.60 |
| GE9D209C | 6.220 | 0.06300 | 0.0017265 | 0.313 | 91.86 | 7.78 | 46.79 ± 2.70 |
| GE9D209D | 6.736 | 0.37444 | 0.0046503 | 0.217 | 80.02 | 1.31 | 44.18 ± 5.50 |
| GE9D209E | 7.089 | 0.03851 | 0.0068588 | 0.111 | 71.44 | 12.72 | 41.53 ± 11.68 |
| | | | | | | Weighted mean: | 46.19 ± 4.60 |

**Sample MU-407b biotite**      J value: 0.004535

| Experiment no. | $^{40}$Ar/$^{39}$Ar | $^{37}$Ar/$^{39}$Ar[1] | $^{36}$Ar/$^{39}$Ar | $^{40}$Ar[2] ($10^{-14}$ mol) | $^{40}$Ar[2] (%) | K/Ca | Apparent age[3] (±2σ Ma) |
|---|---|---|---|---|---|---|---|
| GE9D211B | 9.406 | 0.01413 | 0.0005281 | 0.131 | 98.34 | 34.68 | 75.24 ± 14.74 |
| GE9D211C | 9.320 | 0.00598 | 0.0015530 | 0.034 | 95.07 | 81.99 | 72.14 ± 63.62 |
| GE9D211D | 9.351 | 0.00003 | 0.0046392 | 0.151 | 85.33 | 16259 | 65.08 ± 9.80 |
| GE9D211E | 9.016 | 0.00367 | 0.0050481 | 0.092 | 83.45 | 133.35 | 61.44 ± 17.70 |
| GE9D211F | 8.842 | 0.04966 | 0.0066822 | 0.072 | 77.69 | 9.87 | 56.17 ± 20.02 |

**Sample MU-608 biotite**      J value: 0.004535

| Experiment no. | $^{40}$Ar/$^{39}$Ar | $^{37}$Ar/$^{39}$Ar[1] | $^{36}$Ar/$^{39}$Ar | $^{40}$Ar[2] ($10^{-14}$ mol) | $^{40}$Ar[2] (%) | K/Ca | Apparent age[3] (±2σ Ma) |
|---|---|---|---|---|---|---|---|
| GE9D212A | 8.836 | 0.00167 | 0.0059468 | 0.203 | 80.10 | 293.94 | 57.84 ± 9.32 |
| GE9D212B | 8.915 | 0.05129 | 0.0079998 | 0.163 | 73.52 | 9.55 | 53.63 ± 11.46 |

**Sample MU-702 biotite**      J value: 0.00455

| Experiment no. | $^{40}$Ar/$^{39}$Ar | $^{37}$Ar/$^{39}$Ar[1] | $^{36}$Ar/$^{39}$Ar | $^{40}$Ar[2] ($10^{-14}$ mol) | $^{40}$Ar[2] (%) | K/Ca | Apparent age[3] (±2σ Ma) |
|---|---|---|---|---|---|---|---|
| GE9D313A | 10.005 | 0.02232 | 0.0010606 | 0.336 | 96.88 | 21.96 | 79.03 ± 6.44 |
| GE9D313B | 10.186 | 0.02840 | 0.0021204 | 0.305 | 93.86 | 17.25 | 77.97 ± 6.00 |
| GE9D313C | 9.259 | 0.01811 | 0.0049958 | 0.322 | 84.06 | 27.05 | 63.73 ± 3.76 |
| GE9D313D | 9.821 | 0.03631 | 0.0041726 | 0.244 | 98.76 | 13.49 | 79.09 ± 9.76 |
| GE9D313E | 10.065 | 0.02091 | 0.0041614 | 0.312 | 87.79 | 23.44 | 72.18 ± 6.50 |
| GE9D313F | 11.007 | 0.05701 | 0.0012302 | 0.257 | 96.73 | 8.59 | 86.63 ± 10.18 |

**Sample MU-717 biotite**      J value: 0.00455

| Experiment no. | $^{40}$Ar/$^{39}$Ar | $^{37}$Ar/$^{39}$Ar[1] | $^{36}$Ar/$^{39}$Ar | $^{40}$Ar[2] ($10^{-14}$ mol) | $^{40}$Ar[2] (%) | K/Ca | Apparent age[3] (±2σ Ma) |
|---|---|---|---|---|---|---|---|
| GE9D315A | 7.281 | 0.001703 | 0.0028701 | 0.274 | 88.34 | 287.74 | 52.82 ± 4.48 |
| GE9D315B | 7.134 | 0.016900 | 0.0014995 | 0.259 | 93.79 | 30.62 | 54.92 ± 4.26 |
| GE9D315C | 7.179 | 0.001419 | 0.0009151 | 0.251 | 96.22 | 345.21 | 56.67 ± 4.76 |
| GE9D315D | 7.101 | 0.010155 | 0.0004814 | 0.390 | 97.99 | 48.25 | 57.03 ± 3.26 |
| GE9D315E | 7.162 | 0.014696 | 0.0022953 | 0.336 | 90.53 | 33.34 | 53.24 ± 3.08 |
| GE9D315F | 6.972 | 0.014539 | 0.0017211 | 0.317 | 92.71 | 33.70 | 53.07 ± 4.00 |
| | | | | | | Weighted mean: | 54.85 ± 1.00 |

**Sample MU-717 amphibole**      J value: 0.00455

| Experiment no. | $^{40}$Ar/$^{39}$Ar | $^{37}$Ar/$^{39}$Ar[1] | $^{36}$Ar/$^{39}$Ar | $^{40}$Ar[2] ($10^{-14}$ mol) | $^{40}$Ar[2] (%) | K/Ca | Apparent age[3] (±2σ Ma) |
|---|---|---|---|---|---|---|---|
| GE9D315G | 7.105 | 0.00464 | 0.0018710 | 0.667 | 92.21 | 105.44 | 53.78 ± 2.22 |
| GE9D315H | 7.116 | 0.00308 | 0.0015036 | 0.696 | 93.75 | 159.15 | 54.76 ± 1.76 |
| GE9D315I | 6.962 | 0.00915 | 0.0006617 | 0.721 | 97.19 | 53.54 | 55.52 ± 1.66 |
| GE9D315J | 7.962 | 0.01292 | 0.0039905 | 0.709 | 85.19 | 37.93 | 55.66 ± 2.08 |
| GE9D315K | 7.066 | 0.01485 | 0.0013173 | 0.655 | 94.50 | 32.99 | 54.80 ± 2.40 |
| GE9D315L | 7.068 | 0.01299 | 0.0017652 | 0.608 | 92.62 | 37.72 | 53.74 ± 2.30 |
| | | | | | | Weighted mean: | 54.64 ± 1.66 |

[1] Corrected for $^{37}$Ar and $^{39}$Ar decay, half-lives of 35 d and 259 yr, respectively
[2] Radiogenic argon (nonatmospheric argon)
[3] Ages calculated relative to the Taylor Creek rhyolite (28.34 Ma, Renne et al., 1998)